Monthly Notices of the ROYAL ASTRONOMICAL SOCIETY

MNRAS **497,** 3770–3789 (2020) doi:10.1093/mnras/staa1821
Advance Access publication 2020 July 7

Optical studies of two stripped-envelope supernovae – SN 2015ap (Type Ib) and SN 2016P (Type Ic)

Anjasha Gangopadhyay,[1,2★] Kuntal Misra,[1★] D. K. Sahu,[3] Shan-Qin Wang,[4] Brajesh Kumar,[3] Long Li,[4] G. C. Anupama,[3] Raya Dastidar,[1,5] N. Elias-Rosa,[6,7] Brijesh Kumar,[1] Mridweeka Singh,[1,2,8★] S. B. Pandey,[1] Pankaj Sanwal,[1,2] Avinash Singh,[3,9] S. Srivastav,[10] L. Tartaglia[11] and L. Tomasella[12]

[1]*Aryabhatta Research Institute of Observational Sciences, Manora Peak, Nainital 263002, Uttarakhand, India*
[2]*School of Studies in Physics and Astrophysics, Pandit Ravishankar Shukla University, Raipur 492010, Chhattisgarh, India*
[3]*Indian Institute of Astrophysics, Koramangala, Bangalore 560034, Karnataka, India*
[4]*Guangxi Key Laboratory for Relativistic Astrophysics, School of Physical Science and Technology, Guangxi University, Nanning 530004, People's Republic of China*
[5]*Department of Physics and Astrophysics, University of Delhi, South Campus, South Moti Bagh, Delhi 110007, New Delhi*
[6]*Institute of Space Sciences (ICE, CSIC), Campus UAB, Carrer de Can Magrans S/N, E-08193 Barcelona, Spain*
[7]*Institut d'Estudis Espacials de Catalunya (IEEC), c/Gran Capitá 2-4, Edif. Nexus 201, E-08034 Barcelona, Spain*
[8]*Korea Astronomy and Space Science Institute, 776 Daedeokdae-ro, Yuseong-gu, Daejeon 34055, Republic of Korea*
[9]*Joint Astronomy Programme, Department of Physics, Indian Institute of Science, Bengaluru 560012, Karnataka, India*
[10]*Queen's University, University Rd, Belfast BT7 1NN, UK*
[11]*Department of Astronomy and The Oskar Klein Centre, AlbaNova University Center, Stockholm University, SE-106 91 Stockholm, Sweden*
[12]*INAF Osservatorio Astronomico di Padova, Vicolo dell'Osservatorio 5, I-35122 Padova, Italy*

Accepted 2020 June 15. Received 2020 June 1; in original form 2019 June 20

ABSTRACT

We present the photometric and spectroscopic studies of a Type Ib SN 2015ap and a Type Ic SN 2016P. SN 2015ap is one of the bright ($M_V = -18.04$ mag) Type Ib while SN 2016P lies at an average value among the Type Ic SNe ($M_V = -17.53$ mag). Bolometric light-curve modelling of SNe 2015ap and 2016P indicates that both the SNe are powered by ^{56}Ni + magnetar model with ^{56}Ni masses of 0.01 and 0.002 $M_\odot$, ejecta masses of 3.75 and 4.66 $M_\odot$, spin period P_0 of 25.8 and 36.5 ms, and magnetic field B_p of 28.39 $\times$ 10^{14} and 35.3 $\times$ 10^{14} G, respectively. The early spectra of SN 2015ap show prominent lines of He with a 'W' feature due to Fe complexes while other lines of Mg II, Na I, and Si II are present in both SNe 2015ap and 2016P. Nebular phase [O I] profile indicates an asymmetric profile in SN 2015ap. The [O I]/[Ca II] ratio and nebular spectral modelling of SN 2015ap hint towards a progenitor mass between 12 and 20 $M_\odot$.

Key words: techniques: photometric – techniques: spectroscopic – supernovae: general – supernovae: individual: SNe 2015ap, 2016P – galaxies: individual: IC 1776, NGC 5374 – transients: supernovae.

1 INTRODUCTION

Massive stars undergoing catastrophic explosions at the end of their life are coined as core-collapse supernovae (CCSNe; Woosley & Weaver 1986; Heger et al. 2003; Smartt 2009). Among the group of CCSNe, lie the stripped-envelope (SE-SNe) members called SNe of Type IIb, Ib, and Ic that strip off their outer Hydrogen or Helium layer before the explosion (Clocchiatti & Wheeler 1997). Stripping occurs either due to radiation-driven stellar winds (Puls, Vink & Najarro 2008), heavy mass-loss (Smith & Owocki 2006), or mass-transfer with a companion star (Wheeler & Levreault 1985; Podsiadlowski, Joss & Hsu 1992; Yoon, Woosley & Langer 2010). Classically, Type Ib SNe show He features and Type Ic are devoid of He features (Filippenko 1997). However, studies by Woosley, Langer & Weaver (1995), Dessart et al. (2012), and Cano, Maeda & Schulze (2014) suggest that in Type Ic, either Helium is hidden because of improper excitation due to poor mixing or is completely absent. A small fraction of Type Ic SNe (~4 per cent; Shivvers et al. 2017) show broad absorption lines in their spectra around maximum light with expansion velocities between 15 000 and 30 000 km s^{-1}. These are known as broad-lined Type Ic SNe (BL-Ic). Some of the BL-Ic SNe are linked with gamma-ray bursts (GRBs) and X-ray flashes (XRFs) [for example, SN 1998bw/GRB 980425; Galama et al. (1999), SN 2006aj/XRF 060218; Modjaz et al. (2006)].

A number of studies have been made by several authors to investigate the photometric (Richardson, Branch & Baron 2006; Drout et al. 2011; Cano 2013; Bianco et al. 2014; Pritchard et al. 2014; Taddia et al. 2015; Lyman et al. 2016; Prentice et al. 2016) and spectroscopic properties of SE-SNe (Matheson 2001; Modjaz et al. 2016; Prentice et al. 2019). These studies have shown a wide diversity in terms of both light-curve shapes and spectral features in SE-SNe. The typical rise time of SE-SNe is found to be 10–20 d (Prentice et al. 2019) with a weighted peak absolute magnitude of M_V

★ E-mail: anjashagangopadhyay@gmail.com (AG); kuntal@aries.res.in (KM); yashasvi04@gmail.com (MS)

$= -18.03 \pm 0.06$ mag (Richardson et al. 2006). Lyman et al. (2016) found a considerable spread of ∼3 mag in the absolute magnitude light curves of SE-SNe. Taddia et al. (2018) found a correlation between late-time slopes and $\triangle m_{15}$, which is the decay rate from peak up to 15 d post maximum, suggesting that light curves with initial steeper slopes decline faster at later stages.

The ^{56}Ni mass, ejecta mass, and kinetic energy can be measured by modelling the bolometric light curves. Cano (2013) estimated median ^{56}Ni mass between 0.15 and 0.18 $M_\odot$ and ejecta masses of 3.9 and 3.4 $M_\odot$ for Type Ib and Type Ic SNe, respectively. While Taddia et al. (2018) found ejecta masses for SE-SNe to be between 1.1 and 6.2 $M_\odot$, Prentice et al. (2019) quote the median distribution to be 2.8 ± 1.5 $M_\odot$. Even though high ejecta masses for Type Ic SNe indicate higher progenitor masses, the distribution of ejecta masses for Type Ic SNe hints towards a wide distribution of progenitor masses. Also, the ejecta mass distribution for both Type Ib and Ic SNe is inconsistent with massive single stars and supports moderate-mass stars in binary associations (Lyman et al. 2016). The most common technique used for direct detection of progenitors involves analysing the pre-explosion images. So far, direct detection has been possible for only one Type Ib SN iPTF13bvn (Cao et al. 2013; Groh, Georgy & Ekström 2013; Bersten et al. 2014; Fremling et al. 2014; Kuncarayakti et al. 2015; Eldridge & Maund 2016; Folatelli et al. 2016; Fremling et al. 2016; Hirai 2017a, b) and one Type Ic SN 2017ein (Kilpatrick et al. 2018; Van Dyk et al. 2018). The progenitor masses of iPTF13bvn and SN 2017ein were found to be 10–20 $M_\odot$ (Cao et al. 2013; Groh et al. 2013) and 47–80 $M_\odot$ (Kilpatrick et al. 2018; Van Dyk et al. 2018), respectively, although the progenitor detection of SN 2017ein is debated (Kilpatrick et al. 2018; Van Dyk et al. 2018).

Metallicity and rotation largely affect the predicted ratios of Type Ib/c SNe, mass-loss rates, and the production of WR stars (Eldridge, Izzard & Tout 2008). Eldridge et al. (2008) have shown that stars with high ejecta mass come from massive progenitors. However, if fallback occurs, even less massive stars can eject more mass (for example SN 1999dn; Benetti et al. 2011). Kuncarayakti et al. (2015) favour low-mass binary systems as progenitors of Type Ib/c SNe. On the other hand, Galbany et al. (2018) claimed that Type Ic SNe have the most massive progenitors. However, both Kuncarayakti et al. (2015) and Galbany et al. (2018) suggest the origin of Type Ib/c SNe from young stellar populations. Thus, the exact characterization of ejecta mass, energy, and consecutively the progenitor system remains largely uncertain.

In this paper, we present the photometric and spectroscopic study of a Type Ib SN 2015ap and a Type Ic SN 2016P. The SNe details are given in Section 2. The data acquisition and reduction procedures are described in Section 3. Temporal evolution of the multiband light curves and colour curves is studied in Section 4 along with the analytical modelling of the bolometric light curve. A detailed description of the spectral evolution and asymmetry in the nebular phase are presented in Sections 5 and 6, respectively. Section 7 summarizes the main results of this study.

2 PARAMETERS OF SNE

2.1 SN 2015ap

SN 2015ap was discovered by Lick Observatory Supernova Search on 2015 September 8 by Ross, Zheng, and Filippenko at R.A.= $02^h05^m13.3^s$ and Decl.= $+06^\circ06'08''$ (J2000.0). The SN was located 28.″7 west and 16.″4 south of the centre of the host galaxy IC 1776 at a redshift of 0.01138. The classification spectrum was obtained with Copernico 1.82 m telescope (+AFOSC; range 340–820 nm; resolution 1.4 nm) operated by INAF Astronomical observatory of Padova in Asiago, Mount Ekar, Italy, on 2015 September 11 (Tartaglia et al. 2015) and the spectrum was found to be similar to those of several broad-lined Type Ib/c SNe close to maximum light. It was reclassified as Type Ib SN using the spectrum obtained on 2015 September 21 by Shivvers et al. (2015). We used the GEneric cLAssification TOol (GELATO; Harutyunyan et al. 2008) on the first three spectra of SN 2015ap. GELATO compares bins of the spectrum to those of template SNe at similar epochs, which suggests that the explosion occurred on 2015 September 5 ± 1. However, GELATO results will be reasonable only if the light curves also match. We match the *V*-band light curve of SN 2015ap with the light curves of the SNe in our comparison sample (see Section 4). Performing a template fitting method by applying a simultaneous shift in phase and magnitude, we find that the light curve of SN 2007gr best matches our observed light curve that constrains the explosion epoch as 2015 September 7 ± 1. To further constrain the explosion epoch, we performed a parabolic fit (described in Gangopadhyay et al. 2018) to the *V*-band light curve and infer the explosion epoch to be 2015 September 7. Based on the above methods, we conclude that the explosion occurred between 2015 September 4 and 8. We adopt a distance modulus of $\mu = 33.27 \pm 0.15$ mag for the host galaxy IC 1776 and total $A_V = 0.115$ mag along the line of sight (negligible host extinction) from Prentice et al. (2019).

2.2 SN 2016P

SN 2016P was discovered on 2016 January 19, 21.″7 east and 2.″8 north of the centre of the host galaxy NGC 5374 at R.A. = $13^h57^m31.13^s$ and Dec. = $+06^\circ05'51.6''$ (J2000.0). An optical spectrum obtained with YFOSC at Yunnan Astronomical Observatories on 2015 January 19.9 was found to be consistent with a BL Ic SN a few days before maximum light (Zhang & Wang 2016). Following the same approach as in SN 2015ap, GELATO runs on the first three spectra of SN 2016P estimates the explosion epoch to be 2016 January 15 ± 1. The light-curve template fitting method gives a best match with SN 2007ru and constrains the explosion epoch to be 2016 January 18 ± 3. The parabolic fit to the *V*-band light curve up to 10 d estimates the explosion epoch to be around 2016 January 15 ± 1. The bolometric light-curve modelling (see Section 4.2) gives the explosion epoch to be 2016 January 15. The results of the above methods constrain the explosion epoch to be between 2016 January 14 and 18 (since discovery was on 2016 January 19, we constrain it up to 2016 January 18). From Prentice et al. (2019), we adopt a distance modulus of $\mu = 34.19 \pm 0.15$ mag for the host galaxy NGC 5374. The galactic $E(B-V)$ along the line of sight of SN 2016P is 0.024 mag (Schlafly & Finkbeiner 2011). Using the equivalent width of the NaID line, Prentice et al. (2019) estimate the host galaxy $E(B-V) = 0.05 \pm 0.02$ mag. Due to the poor resolution in our observed spectra, we were unable to measure the equivalent width of the NaID line. We adopt a total extinction of $A_V = 0.229 \pm 0.092$ mag along the line of sight of SN 2016P from Prentice et al. (2019).

3 DATA ACQUISITION AND REDUCTION

Photometric observing campaigns were carried out from 2015 September 18 to 2016 August 27 for SN 2015ap and from 2016 January 21 to 2016 June 3 for SN 2016P using 1.04 m Sampurnanand Telescope (ST), 1.30 m Devasthal Fast Optical Telescope (DFOT) located in ARIES, Nainital, India, Copernico 1.82 m Telescope operated by INAF Astronomical University of Padova (Mount Ekar),

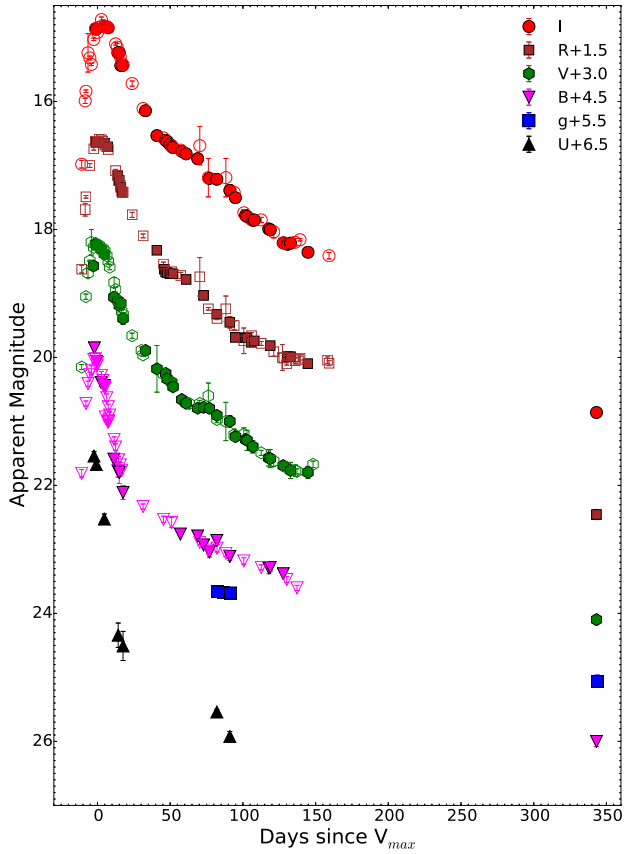

Figure 1. *UgBVRI* light-curve evolution of SN 2015ap. The filled symbols represent our data and open symbols represent the data taken from Prentice et al. (2019).

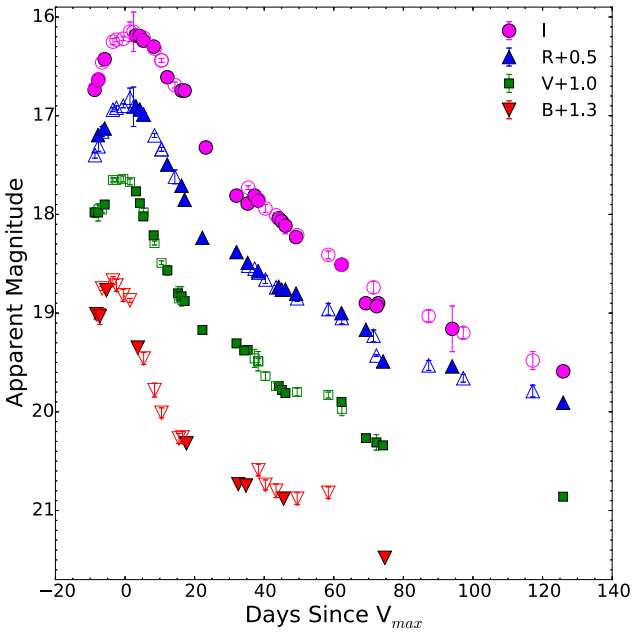

Figure 2. *BVRI* light-curve evolution of SN 2016P. The filled symbols represent our data and open symbols represent the data taken from Prentice et al. (2019).

Italy, 2.00 m Himalayan Chandra Telescope (HCT), IAO, Hanle, India, and 2.54 m Nordic Optical Telescope (NOT), La Palma, Canary Island. The imaging observations were done using Johnson–Cousin–Bessel *UBVRI* and SDSS *ugriz* filters. Image reduction and photometry were done using IRAF[1] and DAOPHOT[2] following the same steps as outlined in Gangopadhyay et al. (2018) and briefly described in Appendix A. The SN magnitudes were calibrated with respect to the local standards (Fig. A1, Tables A1 and A2, available online). The final magnitudes of SNe 2015ap and 2016P are given in Tables A3 and A4, respectively. Low- and medium-resolution optical spectra of SN 2015ap were obtained with 2.0 m HCT and Copernico 1.82 m telescope at 14 epochs. For SN 2016P, spectra were obtained at six epochs with HCT. The spectroscopic reduction was done using standard packages in IRAF. The spectra were wavelength and flux calibrated following the steps described in Gangopadhyay et al. (2018). The log of spectroscopic observations is presented in Tables A5 and A6, available online.

4 TEMPORAL EVOLUTION OF SNE 2015AP AND 2016P

The complete multiband optical light curves of SNe 2015ap and 2016P are shown in Figs 1 and 2, respectively. The date of maximum and brightness at peak in different bands were determined by fitting a cubic spline to the *BVRI* light curve of both the SNe and are listed in Table 1. The maximum in the *V* band for SNe 2015ap and 2016P occurred on MJD 57284.86 ± 0.50 and 57416.75 ± 0.50 at an apparent magnitude of 15.23 ± 0.02 and 16.64 ± 0.08 mag, respectively. The errors reported are obtained from the interpolated measurements around the peak. We notice that there is a gradual delay in reaching the maximum in the redder passbands. We use days since *V*-maximum as a reference epoch throughout the paper.

The light-curve features of SNe 2015ap and 2016P are compared with those of other well-studied SNe Ib/c in Fig. 3. We construct a sample of SNe Ib/c from literature and list their parameters in Table 2. The comparison sample chosen is vast and diverse. While SNe 2009jf and iPTF13bvn are fast evolving, SN 1999dn is a prototypical Type Ib SN. Type Ic sample consists of both normal and BL-Ic's to highlight the diversity in this sub-class. We have also included both fast- and slow-evolving Type Ic that enables us to make a direct comparison with SN 2016P. In addition to these, we have also selected those Type Ib/c SNe from Prentice et al. (2019) that have observations in the *B* and *V* bands that are consistent with our observations. This comparison sample represents the properties of the Type Ib/c population.

Fig. 3 shows the light-curve evolution up to 150 d post *V*-maximum. The observed SN magnitudes of SNe 2015ap and 2016P along with the comparison sample are normalized with respect to their respective peak magnitudes, and a shift in the time is applied to match the time of maximum. To compare the light-curve evolution of Type Ib/c SNe, we estimated decline of the light curve in the first 15 d after peak ($\triangle m_{15}$) and late phase decline rate between 50 and 100 d. The decline rates are listed in Table 3.

Drout et al. (2011) state that the average values of $\triangle m_{15}(V)$ and $\triangle m_{15}(R)$ from a literature sample of Type Ib/c SNe are 0.94 ± 0.31 and 0.74 ± 0.21 mag, respectively. For an individual Type Ib, Ic, and Ic-BL sample, Drout et al. (2011) estimate $\triangle m_{15}(R)$ to be 0.7 ± 0.1, 0.9 ± 0.5, and 0.7 ± 0.1 mag. The $\triangle m_{15}(V)$ value of SN 2015ap

[1]Image Reduction and Analysis Facility.
[2]Dominion Astrophysical Observatory Photometry.

Table 1. Parameters of SNe 2015ap and 2016P.

SN 2015ap	*B* band	*V* band	*R* band	*I* band
MJD (maximum)	57283.0 ± 0.5	57284.9 ± 0.5	57289.3 ± 0.5	57287.5 ± 0.5
Magnitude at maximum (mag)	15.54 ± 0.03	15.23 ± 0.02	15.16 ± 0.02	14.76 ± 0.04
Absolute magnitude at maximum (mag)	− 17.71 ± 0.19	− 18.04 ± 0.19	− 18.15 ± 0.17	− 18.54 ± 0.16
Δm_{15} (mag)	1.73 ± 0.10	1.03 ± 0.07	0.74 ± 0.05	0.58 ± 0.05
Rise time (rest-frame-day)	9.9	11.8	16.1	14.3
SN 2016P	*B* band	*V* band	*R* band	*I* band
MJD (maximum)	57413.03 ± 0.5	57416.75 ± 0.5	57417.20 ± 0.5	57418.36 ± 0.5
Magnitude at maximum (mag)	17.37 ± 0.05	16.64 ± 0.08	16.36 ± 0.08	16.15 ± 0.05
Absolute magnitude at maximum (mag)	− 16.89 ± 0.12	− 17.53 ± 0.14	− 17.81 ± 0.13	− 17.92 ± 0.11
Δm_{15} (mag)	1.47 ± 0.12	1.20 ± 0.06	0.93 ± 0.04	0.63 ± 0.05
Rise time (rest-frame-day)	6.9	10.6	11.0	12.4

matches well with iPTF13bvn, and is higher than the value quoted in Drout et al. (2011) but is consistent with the values reported in Taddia et al. (2018). The Δm_{15} values in SN 2016P are in between those of the Type Ic comparison sample used in this work; however, they are a bit faster than the average values reported in Drout et al. (2011) and Taddia et al. (2018). The late-time light curves are faster than the average decay rate of ^{56}Co to ^{56}Fe. Taddia et al. (2018) estimated the late-time decay rates between 1.4–1.8 mag (100 d)$^{-1}$ and 1.7–2.7 mag (100 d)$^{-1}$ for Type Ib and Type Ic sample, respectively. Table 3 and Fig. 3, thus, show that both SNe 2015ap and 2016P show faster evolution than the ^{56}Co to ^{56}Fe decay rates. This implies inefficient gamma-ray trapping for both the SNe.

4.1 Colour evolution of SNe 2015ap and 2016P

The colour evolution of SNe 2015ap and 2016P along with other members of the comparison sample is displayed in Fig. 4. A diversity exists among the colour variation due to the expansion of photospheric envelope and the changing temperatures. All the colour curves have been dereddened by the value reported in Table 2. The pre-maximum $(B - V)_o$ colours of all the SNe are similar and bluer, which occurs due to the increase in photospheric temperatures as SN brightens. From −11 to 2 d, the $(B - V)_o$ colours of SN 2015ap increase from 0.12 to 0.61 mag. During the maximum light, the $(B - V)_o$ colour remains around 1.1 mag and becomes bluer post 100 d. The $(B - V)_o$ colour evolution of SN 2015ap is similar to all the SNe of Type Ib comparison sample. A similar trend is noticed for the $(V - R)_o$ colours of SN 2015ap that is blue (∼0.03 mag) at pre-maximum and becomes redder with time. Drout et al. (2011) found that the average $(V - R)_o$ colour 10 d post *V*-maximum should be around 0.26 ± 0.10 mag for Type Ib/c SNe, if the estimated extinction is well within errors. The $(V - R)_o$ colour of SN 2015ap is between 0.25 and 0.35 mag around 10 d post *V*-maximum that is well in agreement with the values of Drout et al. (2011). A similar trend is noticed for the $(V - I)_o$ colours of SN 2015ap that becomes redder as we move to maximum and remains constant thereafter.

The $(B - V)_o$ colour evolution of SN 2016P increases from 0.6 to 1.2 mag 10 d after *V*-maximum. The $(V - R)_o$ colours of SN 2016P become redder increasing from 0.2 to 0.6 mag. Dessart et al. (2016) and Drout et al. (2011) have found that the $(V - R)_o$ colours 10 d post *V*-maximum show an average scatter ranging between 0.18 and 0.34 mag. At similar epochs, our value of $(V - R)_o \sim 0.62$ mag indicates the SN to be intrinsically redder. The $(V - I)_o$ colours of SN 2016P follow similar trend as $(V - R)_o$ that increases up to 1 mag. Post 100 d, the $(V - I)_o$ colour becomes blue. SN 2016P is redder than most of the Type Ic SNe comparison sample. This indicates either the presence of absorbers in the system or the SN is intrinsically red.

4.2 Absolute magnitude and Bolometric light curves

Fig. 5 shows the absolute magnitude light curves of SNe 2015ap and 2016P along with other members of the sub-class that are corrected for extinction and reddening values reported in Table 2. The peak absolute magnitudes of SNe 2015ap and 2016P are listed in Table 1. The absolute magnitudes of SN 2015ap in the *V* and *R* bands are −18.04 ± 0.19 and −18.15 ± 0.17 mag, respectively, which are comparable with the average distribution of Type Ib SNe (−17.98 ± 0.13 mag; Richardson et al. 2006, −17.9 ± 0.9 mag; Drout et al. 2011). As compared with the recent results by Taddia et al. (2018), the average value of Type Ib SNe to be −17.07 ± 0.56, *V*-band absolute magnitude of SN 2015ap is brighter by ∼0.5 mag. The *V*-band absolute magnitude light curve of SN 2015ap shows that it is one of the bright SNe among the Type Ib SNe used for comparison. The *R*-band absolute magnitude of SN 2016P is ∼0.5 mag fainter than the sample of Type Ic SNe (−18.3 ± 0.6; Drout et al. 2011). The *V*-band absolute magnitude is also fainter than the sample of Type Ic by 1 mag (−18.51 ± 0.10 mag; Richardson et al. 2006) while the values are consistent with the recent results by Taddia et al. (2018). Table 2 shows that SN 2015ap lies among the brighter end of the Type Ib comparison sample while SN 2016P is of average brightness object among the Type Ic comparison sample.

We constructed the bolometric light curves of SNe 2015ap and 2016P using blackbody (BB) fitting model. The bolometric light curves were constructed by using the photometric data of at least three filters to fit BB spectral energy distribution. For SN 2015ap, however, we also used the pre-peak data of two filters since we need pre-peak bolometric light curve to pose more stringent constraint on the explosion epoch. Neglecting the dilution effect of the ejecta (Dessart et al. 2012) and assuming that the SN emission is mostly BB, we estimated the BB temperature (T) and photospheric radius (R_{ph}) as free parameters of our code. We neglect the blue-ultraviolet (UV) suppression that yields lower UV and bright optical luminosities. Using the values of T and R_{ph}, obtained through BB fitting and considering the contribution of far-UV and far-IR emission, we estimated the bolometric luminosities using the formula $4\pi R_{ph}^2 \sigma T^4$. However, in reality, the spectra of SNe Ib/c are not blackbodies and there is substantial deviation from this at early and late times due to line blanketing and line emission/loss of photosphere, respectively. With the assumption that the photospheric velocity (v_{ph}) is equal

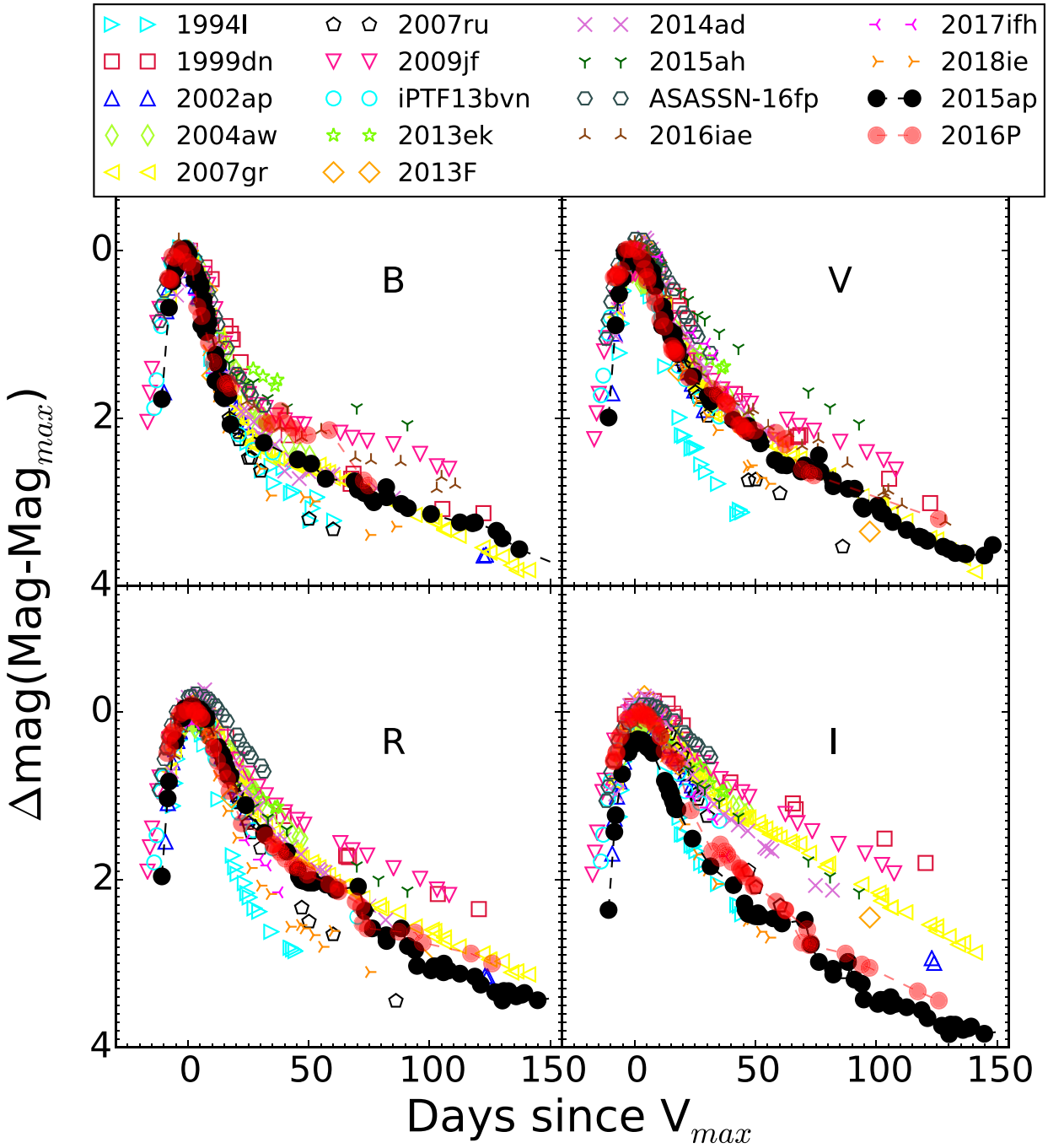

Figure 3. *BVRI/ri* light-curve evolution of SN 2015ap and SN 2016P compared with other members of the sub-class. All the light curves are shifted in phase and matched to maximum light.

to the scale velocity (v_{sc}), we have modelled the light curves of both the SNe. The photospheric velocity values are taken from the SYN++ modelling of the spectrum done in Section 5. We have constrained the priors in the code to obtain physical values of the obtained parameters. In order to fit the bolometric light curves of SNe 2015ap and 2016P, we used Markov chain Monte Carlo simulations on the light curves to obtain the best-fitting parameters. The optical opacity is fixed to be 0.07 cm^2 g^{-1}, which is justified if electron scattering opacity is the dominant source (see for example, Taddia et al. 2018).

^{56}Ni model: With the assumption that the bolometric luminosity is powered by the decay of ^{56}Ni to ^{56}Co and ^{56}Co to ^{56}Fe, we fit the bolometric light curves using the ^{56}Ni model. The ^{56}Ni model was constructed taking into account the assumptions of Arnett (1982) and Chatzopoulos, Wheeler & Vinko (2012). The employed free parameters of the ^{56}Ni model are the ejecta mass M_{ej}, ^{56}Ni mass M_{Ni}, gamma-ray opacity of ^{56}Ni decay photons $\kappa_{\gamma,Ni}$, and explosion time t_{expl}. Following Arnett (1982), τ determines the width of the bolometric light curve and can be expressed in terms of opacity (κ), ejecta mass M_{ej}, and the photospheric velocity at luminosity peak

Table 2. Properties of the comparison sample.

SNe	Host galaxy	Distance (Mpc)	Extinction $E(B-V)$	SN type	Peak Absmag[b] V band	M_{Ni} ($M_\odot$)	M_{ej} ($M_\odot$)	E_k 10^{52} erg	Reference[a]
SN 1999dn	NGC 7714	38.5	0.100	Ib	−16.88	0.09 ± 0.04	5.13 ± 1.82	0.37 ± 0.13	2, 11, 12
SN 2009jf	NGC 7479	33.7	0.110	Ib	−17.90	0.18 ± 0.04	7.34 ± 1.0	1.05 ± 0.15	4, 11
iPTF 13bvn	NGC 5806	23.9	0.215	Ib	−17.35	0.09	1.5–2.2	0.1	5
SN 2013ek	NGC 6984	50.1	0.037	Ib	−17.22	0.05 ± 0.01	1.2	0.04	13
SN 2015ah	UGC12295	58.9	0.091	Ib	−17.53	0.092 ± 0.07	2	0.09	13
SN 1994I	M51	6.3	0.452	Ic	−17.49	0.06 ± 0.01	0.72 ± 0.04	0.07 ± 0.01	1, 11, 12
SN 2002ap	NGC 0628	9.9	0.090	Ic-BL	−18.11	0.09	≥1.5	–	6
SN 2004aw	NGC 3997	72.8	0.092	Ic	−17.30	0.22 ± 0.08	6.49 ± 2.32	0.90 ± 0.32	7, 11, 12
SN 2007gr	NGC 1058	9.7	0.092	Ic	−17.11	0.04 ± 0.01	1.70 ± 0.23	0.08 ± 0.01	3, 11, 12
SN 2007ru	UGC 12381	64.2	0.270	Ic-BL	−18.92	0.34 ± 0.09	3.59 ± 1.52	1.43 ± 0.57	8, 11, 12
SN 2013F	IC 5325	17.6	1.418	Ic	−18.55	0.15	1.4	0.11	13
SN 2014ad	MRK 1309	26.6	0.220	Ic-BL	−18.72	0.24	3.3 ± 0.8	1 ± 0.3	9, 12
ASASSN-16fp	NGC 5806	23.9	0.074	Ic	−18.36	0.1	4.5 ± 0.3	0.69	10, 12
SN 2016iae	NGC 1532	17.3	0.664	Ic	−18.23	0.13	2.2	0.18	13
SN 2017ifh	2MASX J06350438+5026278	156.3	0.167	Ic-BL	−18.55	0.16 ± 0.01	3.0	0.77	13
SN 2018ie	NGC 3456	46.8	0.08	Ic-BL	−16.94	0.026 ± 0.002	1.5	0.79	13

Notes. [a]References – (1) Richmond et al. (1996); (2) Benetti et al. (2011); (3) Hunter et al. (2009); (4) Sahu et al. (2011), NED; (5) Srivastav, Anupama & Sahu (2014), NED; (6) Yoshii et al. (2003), Foley et al. (2003), NED; (7) Taubenberger et al. (2006), NED; (8) Sahu et al. (2009); (9) Sahu et al. (2018); (10) Kumar et al. (2018); (11) Cano (2013); (12) NED; (13) Prentice et al. (2019).
[b]Values are scaled with respect to $H_o = 73$ km s^{-1} Mpc^{-1}.

Table 3. Early- and late-time decay rates of a sample of Type Ib/c SNe.

Supernova	$\triangle m_{15}$ (mag)		Late-time (50–100 d) decay rates [mag (100 d)$^{-1}$]				Reference[a]
	V	R	B	V	R	I	
SN 1999dn	0.49 ± 0.08	0.31 ± 0.03	1.07 ± 0.19	1.54 ± 0.09	1.32 ± 0.09	1.15 ± 0.07	3
SN 2007gr	1.31 ± 0.05	0.46 ± 0.07	1.11 ± 0.06	1.70 ± 0.05	1.94 ± 0.07	1.64 ± 0.04	3, 1
SN 2009jf	0.50	0.31	0.89 ± 0.14	1.36 ± 0.07	1.61 ± 0.02	1.71 ± 0.11	4, 5
iPTF13bvn	1.01	0.90	–	–	–	–	10
SN 2013ek	0.78 ± 0.08	0.60 ± 0.10	–	–	–	–	12, 3
SN 2015ah	0.83 ± 0.04	0.71 ± 0.01	–	–	–	–	12, 3
SN 2015ap	1.03 ± 0.07	0.74 ± 0.05	1.10 ± 0.15	1.55 ± 0.14	2.14 ± 0.18	1.88 ± 0.17	3
SN 1994I	1.74 ± 0.02	1.46 ± 0.02	–	1.84 ± 0.05	–	–	2
SN 2002ap	1.85 ± 0.45	–	1.70 ± 0.04	2.10 ± 0.02	1.60 ± 0.01	1.70 ± 0.01	3, 6
SN 2004aw	0.62 ± 0.03	0.41 ± 0.03	1.35 ± 0.18	1.74 ± 0.22	1.36 ± 0.14	1.53 ± 0.19	5
SN 2007ru	0.92	0.69	–	2.1	2.8	3.0	7
SN 2013F	1.43 ± 0.26	1.05 ± 0.28	–	–	–	–	12, 3
SN 2014ad	0.95 ± 0.06	0.77 ± 0.03	0.89 ± 0.10	2.19 ± 0.13	2.17 ± 0.05	2.04 ± 0.11	3, 8
ASASSN-16fp	0.60 ± 0.02	0.42 ± 0.02	–	–	–	–	3, 9
SN 2016iae	0.91 ± 0.25	–	1.29 ± 0.24	1.61 ± 0.19	–	–	12, 3
SN 2018ie	1.41 ± 0.16	1.06 ± 0.13	–	–	–	–	12, 3
SN 2016P	1.20 ± 0.06	0.93 ± 0.04	–	1.75 ± 0.22	1.78 ± 0.18	2.09 ± 0.21	3
Type Ib/c, Ic-BL	0.94 ± 0.31	0.74 ± 0.21	–	–	–	–	11
Type Ib SNe	1.03 ± 0.19	0.75 ± 0.21	–	–	–	–	13
Type Ic SNe	0.90 ± 0.22	0.62 ± 0.24	–	–	–	–	13

Notes. [a]References – (1) Hunter et al. (2009); (2) Richmond et al. (1996); (3) This work; (4) Taubenberger et al. (2006); (5) Valenti et al. (2011), Sahu et al. (2011); (6) Hunter et al. (2009); (7) Sahu et al. (2009); (8) Sahu et al. (2018); (9) Kumar et al. (2018); (10) Srivastav et al. (2014); (11) Drout et al. (2011); (12) Prentice et al. (2019); (13) Taddia et al. (2018).

v_{ph}:

$$\tau_m = \sqrt{2}\left(\frac{k}{\beta c}\right)^{\frac{1}{2}}\left(\frac{M_{ej}}{v_{ph}}\right)^{\frac{1}{2}}, \quad (1)$$

where $\beta = 13.8$ is a constant of integration (Arnett 1982) and c is the speed of light. The kinetic energy for spherically symmetric ejecta with a uniform density is

$$E_k = \frac{3}{10} M_{ej} v_{ph}^2. \quad (2)$$

The best-fitting parameters of the model are tabulated in Table 4 and the best-fitting ^{56}Ni model of SNe 2015ap and 2016P is displayed in Fig. 6. The associated corner plots showing confidence level of different parameters are shown in Figs 7 and 8, respectively. For SN 2015ap, the ^{56}Ni model is able to reproduce the peak luminosity; however, it underestimates the luminosity at late times. Similarly, for SN 2016P the ^{56}Ni model fails to reproduce the luminosity around peak and is a good match to the observed data at late times. In both the SNe, this indicates that ^{56}Ni may not alone be the powering

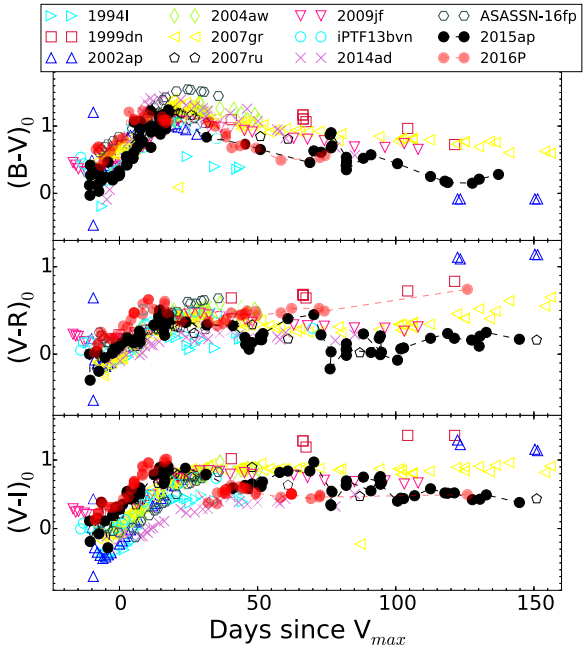

Figure 4. A comparison of the $(B-V)_0$, $(V-R)_0$, and $(V-I)_0$ colours of SNe 2015ap and 2016P with other representative SNe Ib/c. The colours are corrected for the reddening values given in Table 2.

source and an additional source of energy is required to generate the observed luminosity.

^{56}Ni + Magnetar model: One of the most prevailing models adopted to model the light curves of SNe that cannot be explained by the ^{56}Ni model is the magnetar model (Inserra et al. 2013; Wang et al. 2015a). However, as pointed out by Nomoto, Kobayashi & Tominaga (2013), the CCSNe can yield ≤ 0.2 M$_\odot$ of ^{56}Ni and the luminosity produced by ^{56}Ni decay cannot be neglected in modelling the SNe whose peak luminosities are not very high. Therefore, a hybrid model taking into account the contribution from a newly born magnetar and a moderate amount of ^{56}Ni could be a promising model for SNe 2015ap and 2016P. We try to fit the light curves of both SNe 2015ap and 2016P using the ^{56}Ni + Magnetar model (Wang et al. 2015b). The free parameters of the ^{56}Ni + magnetar model are κ, $M_{\rm ej}$, magnetic field $B_{\rm p}$, the initial rotational period P_0, the gamma-ray opacity of magnetar photons $\kappa_{\gamma,\rm mag}$, the gamma-ray opacity of ^{56}Ni cascade decay photons $\kappa_{\gamma,\rm mag}$, and $t_{\rm expl}$.

The best-fitting light curves are shown in Fig. 9 and the parameters are tabulated in Table 4. The associated corner plots showing confidence level of different parameters are also shown in Figs 10 and 11, respectively. Even though the obtained ^{56}Ni mass is low as compared to its kinetic energy, the ^{56}Ni + magnetar model shows good fits to the overall light curves of both the SNe. The uncertainties and the confidence of determination of the parameters as well as the degeneracy and correlation between parameters are shown in the corner plots. However, we remark that the values of ejected mass and the derived kinetic energy depend on the adopted value of opacity.

5 SPECTROSCOPIC EVOLUTION

Our spectroscopic observations of SN 2015ap started 14 d before *V*-maximum and continued up to 125 d post maximum while the spectral coverage of SN 2016P is limited to 28 d after *V*-maximum.

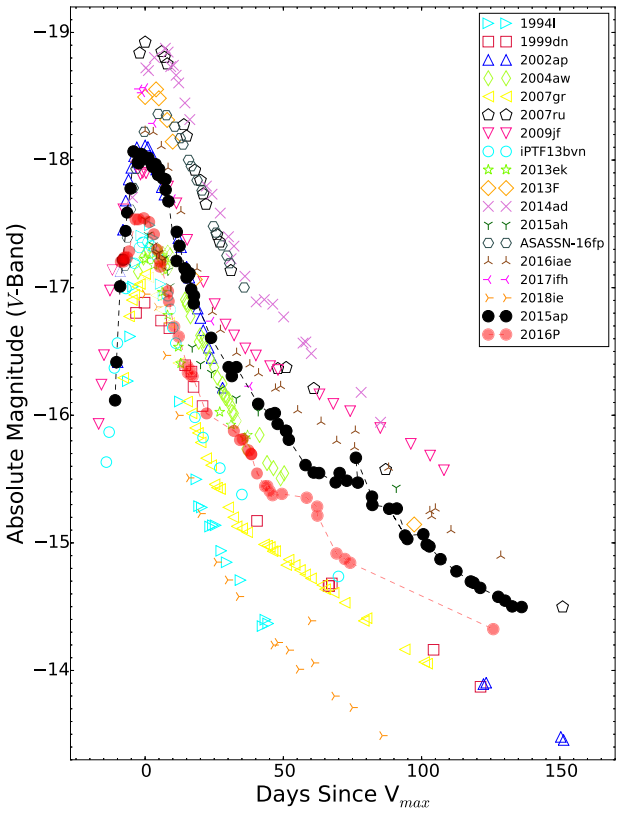

Figure 5. Absolute magnitude *V*-band light curves of SNe 2015ap and 2016P compared to other members of the sub-class. The light curves have been corrected for distance and extinction given in Table 2.

We explain in detail the spectroscopic features of these two events below.

5.1 Spectral evolution of SNe 2015ap and 2016P during early phase

The pre-maximum spectral evolution of SN 2015ap is shown in Fig. 12. The early-time spectral sequence of SN 2015ap shows a blue continuum. Initial few spectra show distinct, blueshifted and broad P Cygni profiles, which is indicative of very high velocities. However, we remark that since SN 2015ap exploded close to H II region, there is contamination of host C II and S II contamination lines. Moreover, around 5000 Å we see significant contamination by H β and [O III] galaxy lines. In the -1.1 d spectrum of SN 2015ap, He I 5876 Å absorption feature expanding with a velocity of $\sim$15 500 km s^{-1} is seen. Other prominent spectral features noticed in the early-time spectra are Fe II between 4100 and 5000 Å, Si II/H α at $\sim$6250 Å, and O I 7774 Å. The He I 4471 Å line is present but with a possible blend of Fe II complexes and Mg II 4481 Å. Except 5015 Å feature, all other He I lines at 4471, 5876, 6678, and 7065 Å are prominent. The spectra taken at 5 and 7 d of SN 2015ap in Fig. 12 show 'W'-shape absorption feature around 4000 Å. A similar kind of feature was observed in Type II SN 2005ap (Quimby et al. 2007), Type Ib SN 2008D (Modjaz et al. 2009), SN 2009jf (Sahu et al. 2011), and Type IIb SN 2001ig (Silverman et al. 2009) but at very early epochs (between -14 and -10 d). While Mazzali et al. (2008) claim the origin of this feature due to Fe complexes, Modjaz et al. (2009) and Silverman et al. (2009) consider this feature to be

Table 4. Parameters of the various models. The uncertainties are 1σ.

	κ ($cm^2\ g^{-1}$)	v_{sc} (10^9 cm s^{-1})	M_{ej} ($M_\odot$)	M_{Ni} ($M_\odot$)	P_0 (ms)	B_p (10^{14} G)	$\kappa_{\gamma,Ni}$ ($cm^2\ g^{-1}$)	$\kappa_{\gamma,mag}$ ($cm^2\ g^{-1}$)	t_{expl} [a] (d)	χ^2/d.o.f.
SN 2015ap										
^{56}Ni	0.07	1.6	$3.73^{+0.02}_{-0.02}$	$0.26^{+0.00}_{-0.00}$	–	–	$0.032^{+0.001}_{-0.001}$	–	$-15.86^{+0.13}_{-0.13}$	113.64/72
magnetar+^{56}Ni	0.07	1.6	$3.90^{+0.21}_{-0.15}$	$0.01^{+0.00}_{-0.00}$	$25.85^{+0.50}_{-0.67}$	$28.39^{+1.64}_{-1.66}$	$0.26^{+0.05}_{-0.04}$	$14.26^{+24.59}_{-8.49}$	$-13.17^{+0.20}_{-0.21}$	10.87/69
SN 2016P										
^{56}Ni	0.07	1.5	$4.66^{+2.09}_{-2.07}$	$0.12^{+0.02}_{-0.02}$	–	–	$0.02^{+0.02}_{-0.01}$	–	$-22.39^{+5.07}_{-4.92}$	12.57/38
magnetar+^{56}Ni	0.07	1.5	$5.13^{+1.03}_{-1.03}$	$0.002^{+0.006}_{-0.004}$	$36.51^{+2.16}_{-2.31}$	$35.30^{+5.25}_{-3.60}$	$1.82^{+17.94}_{-1.66}$	$1.19^{+13.09}_{-1.11}$	$-16.31^{+1.32}_{-1.47}$	3.18/35

Note. [a]The value of t_{expl} is with respect to the date of the first *R*-band observation; the lower limit is set to be −30 here.

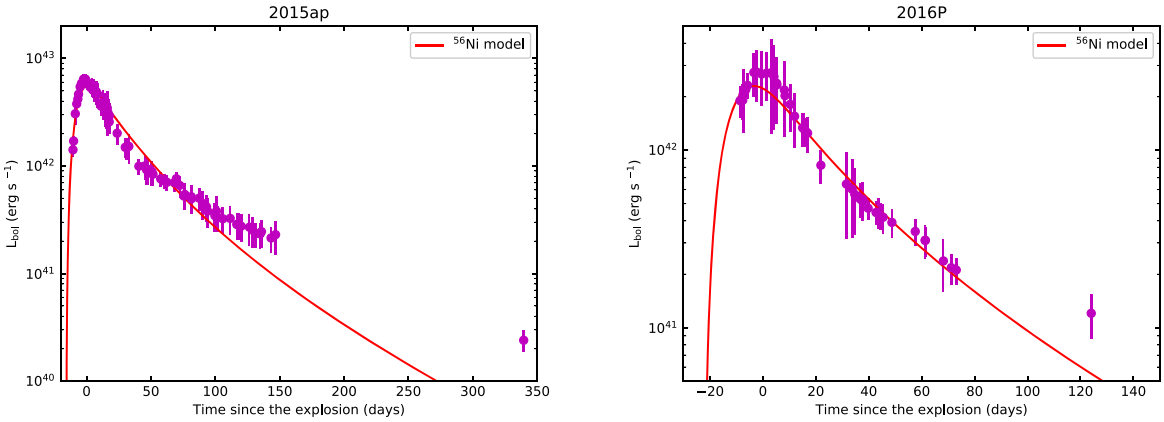

Figure 6. The bolometric light curves of SNe 2015ap (the left-hand panel) and 2016P (the right-hand panel) reproduced by the ^{56}Ni model. The abscissa represents time since the explosion in rest frame. The open circles are derived using two band data while filled circles are derived using three or four band data.

originated due to the C III, N III, and O III lines at high velocities. Since we see the feature in post-maximum phases, we consider the feature to be originated due to Fe complex with a blend of Mg II. The observed spectrum of SN 2015ap is compared with a synthetic spectrum generated using SYN++ (Thomas, Nugent & Meza 2011) as shown in the bottom panel of Fig. 12. The synthetic spectrum with a photospheric temperature of 13 000 K and a photospheric velocity of v_{ph} = 16 000 km s^{-1} reproduces the spectrum of SN 2015ap obtained at −1.1 d. The He I lines are moving with an expansion velocity of ∼15 500 km s^{-1}. Prentice et al. (2019) also estimated the He I 5876 Å line velocities between −10 and 20 d post bolometric maximum that varied between 16 000 to 11 000 km s^{-1}, which is in agreement with our results. We performed a BB fit on the −1.1 d spectrum of SN 2015ap resulting in a temperature estimate of 12 000 ± 2000 K. Prentice et al. (2019) also estimated the temperature variations between −10 and 40 d post bolometric maximum and found those to vary between 11 000 and 5000 K. Their estimated value of temperature is well within the errors of our estimates using BB fit. Fig. 13 shows the evolution of SN 2015ap from 26 to 124 d post maximum. We see that the broad He I absorption feature has decreased with time. Also, the blue continuum has decreased implying a decrease in photospheric temperature. All other spectral lines become prominent and well developed. The He I line around 5876 Å may be blended with Na I 5890, 5896 Å. Post 90 d, we see distinct [O I] 6300, 6364 Å doublet in the spectra of SN 2015ap that marks the onset of nebular phase. We notice prominent [O I] 6300, 6364 Å and [Ca II] 7291, 7324 Å doublet feature in Fig. 13 after this phase. Other identified lines in the spectra include Mg I] 4571 Å feature, O I 7774 Å blended with contributions from O I 8446 Å. We see multipeaked [O I] in the nebular phase spectra of SN 2015ap that is indicative of a highly asymmetric ejecta configuration that will be discussed in detail in Section 6.

Fig. 14 shows spectral sequence of SN 2016P covering a phase range of (−5) – (22)d post *V*-maximum. The 0.1 d spectrum shows a blue continuum. Prominent lines of Mg II, multiplets of Fe II, Si II, O I, and Ca II NIR features are seen in the spectrum. In the spectral sequence, we see two shallow absorption features at 5100 and 5500 Å. The shallow absorption at 5150 Å was noticed as an unidentified feature for Type Ic SN 2004aw (Taubenberger et al. 2006). The broad absorption feature post 6000 Å is believed to have several origins. The feature is thought to be associated with Si II 6355 Å (Foley et al. 2003; Valenti et al. 2008a; Hunter et al. 2009; Sahu et al. 2009; Pignata et al. 2011; Kumar et al. 2018). This absorption feature is also seen in SN 2007gr (Valenti et al. 2008b), SN 2004aw (Taubenberger et al. 2006), and SN 2013ge (Drout et al. 2016). For SNe 2004aw and 2013ge, the feature is considered due to C II 6580 Å. The absorption dip at 5500 Å may result from a possible blending of Na I along with He I features (Pandey et al. 2003; Valenti et al. 2008a; Sahu et al. 2009). To the first three spectra of SN 2016P, we fit SYN++ model. The dotted lines in Fig. 14 show the best-fitting SYN++ model that is moving with a photospheric velocity of v_{ph} = 15 000 km s^{-1} and a temperature of 8000 K that fits the first spectrum well. As we move to the third spectrum, v_{ph} = 13 000 km s^{-1} is achieved with temperatures reaching up to 7000 K. Prentice et al. (2019) also show that at similar epochs, photospheric temperature of SN 2016P is 8000 K. Prominent lines of Si II, Fe multiplets, and Ca lines are

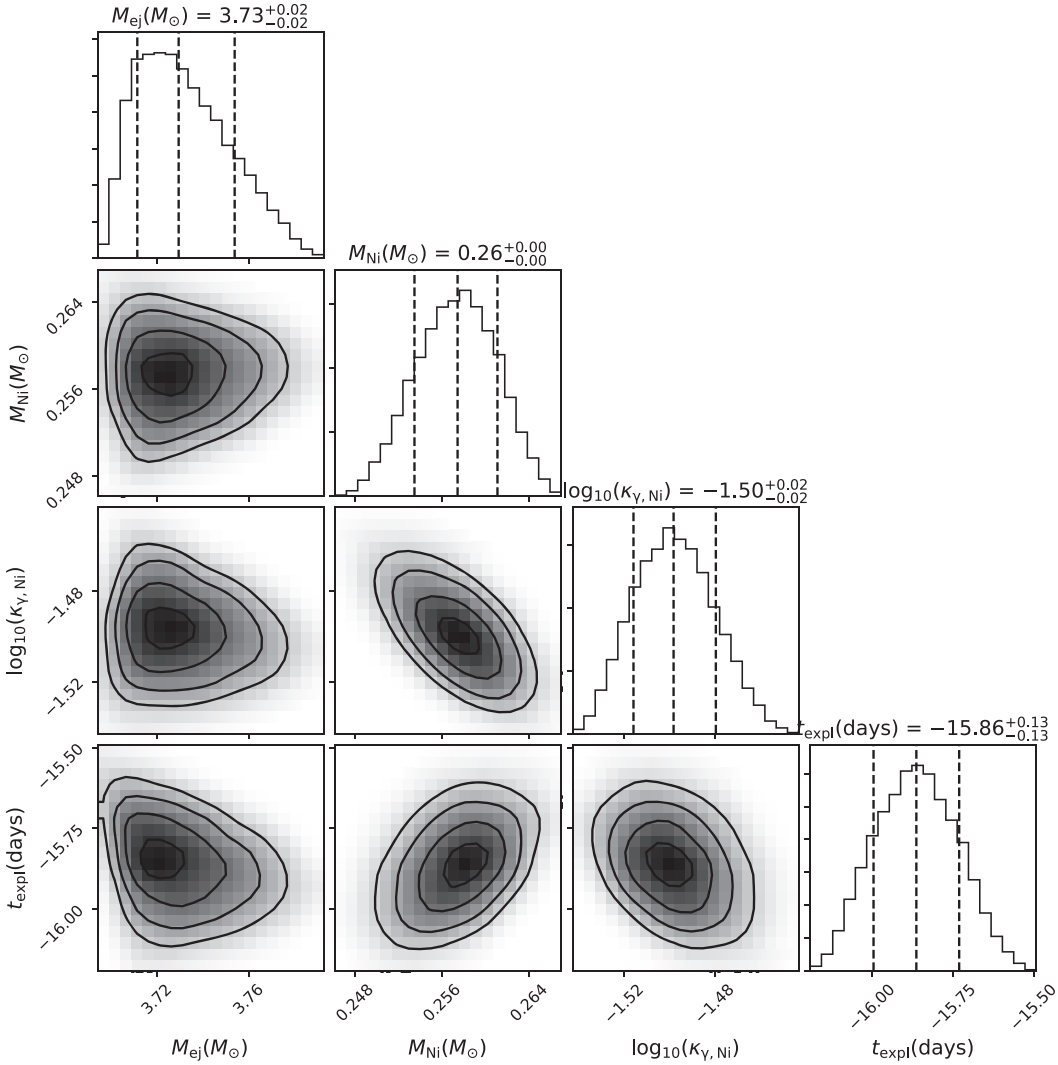

Figure 7. Corner plot of SN 2015ap showing the parameters (M_{ej}, M_{Ni}, κ_γ, t_{expl}) of the ^{56}Ni model.

also well reproduced. Si II lines show a velocity of 10 000 km s^{-1} well in agreement with Prentice et al. (2019).

5.2 Spectral comparison among SE-SNe

The comparison of the pre-maximum spectrum of SN 2015ap is shown in Fig. 15. The −1.1 d spectrum of SN 2015ap shows a distinct blue continuum as compared to all other SNe indicating higher temperatures. This is also in agreement with the results reproduced by SYN++ fitting. He I absorption lines are well established in all the spectra.

We compare the ∼25 d spectra of SNe 2015ap and 2016P with a number of Ib, Ic, Ic-BL, and transitional Ic SNe in Fig. 16. The spectrum of SN 2015ap bears a close resemblance with SN 2009jf. Prominent He I 5876 Å features are seen in the whole sample of Type Ib SN. The He I features in SN 2015ap are very similar to SN 2009jf. The overall spectrum of SN 2016P (at 22 d) is quite similar to SN 2012ap. Prominent Mg II features at other wavelengths along with Mg II + O I at 9000 Å are well developed as compared to all other SNe of the comparison sample. The absorption dip close to 6200 Å is also found to be similar to that of SN 2012ap. The overall spectra of SN 2016P show lines having width in between Type Ic and Ic-BL SNe.

Fig. 17 shows the nebular phase comparison spectra of SN 2015ap along with other Type Ib SNe. SN 2015ap shows an asymmetric emission profile of [O I] as compared to other SNe. Also, the [Ca II] doublet is broad and dispersed than others. This has several implications on the physical scenario that we will explain in detail in Section 6.

6 ASYMMETRY IN THE NEBULAR PHASE EMISSION OF SN 2015AP

As the nebular phase probes deeper into the ejecta, several studies on the ejecta geometry and associated asymmetries have been done in the past (Mazzali et al. 2005; Maeda et al. 2008; Modjaz et al. 2008; Taubenberger et al. 2009; Milisavljevic et al. 2010). The most-prominent lines in nebular phase to study ejecta geometry are [O I] 6300, 6364 Å doublet, [Ca II] 7291, 7324 Å doublet, and the Mg I] 4571 Å lines. However, [O I] is best to probe asymmetry

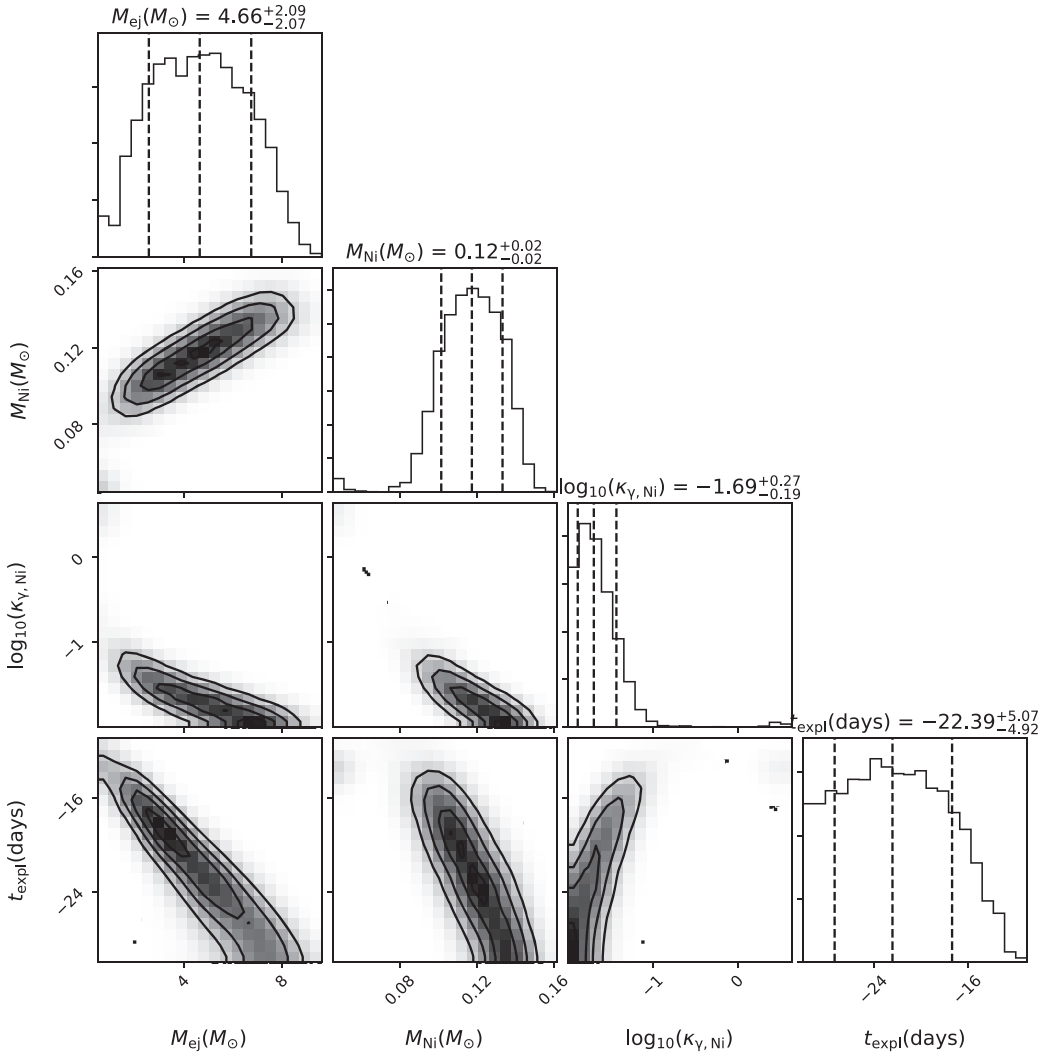

Figure 8. Corner plot of SN 2016P showing the parameters (M_{ej}, M_{Ni}, κ_γ, t_{expl}) of the ^{56}Ni model.

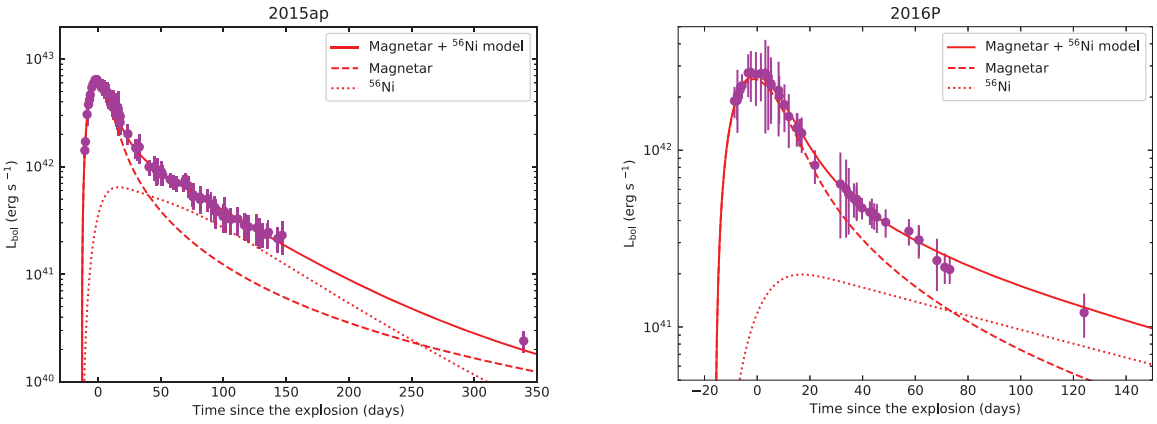

Figure 9. The bolometric light curves of SNe 2015ap (the left-hand panel) and 2016P (the right-hand panel) reproduced by the Magnetar + ^{56}Ni model (the right-hand panel). The abscissa represents time since the explosion in rest frame.

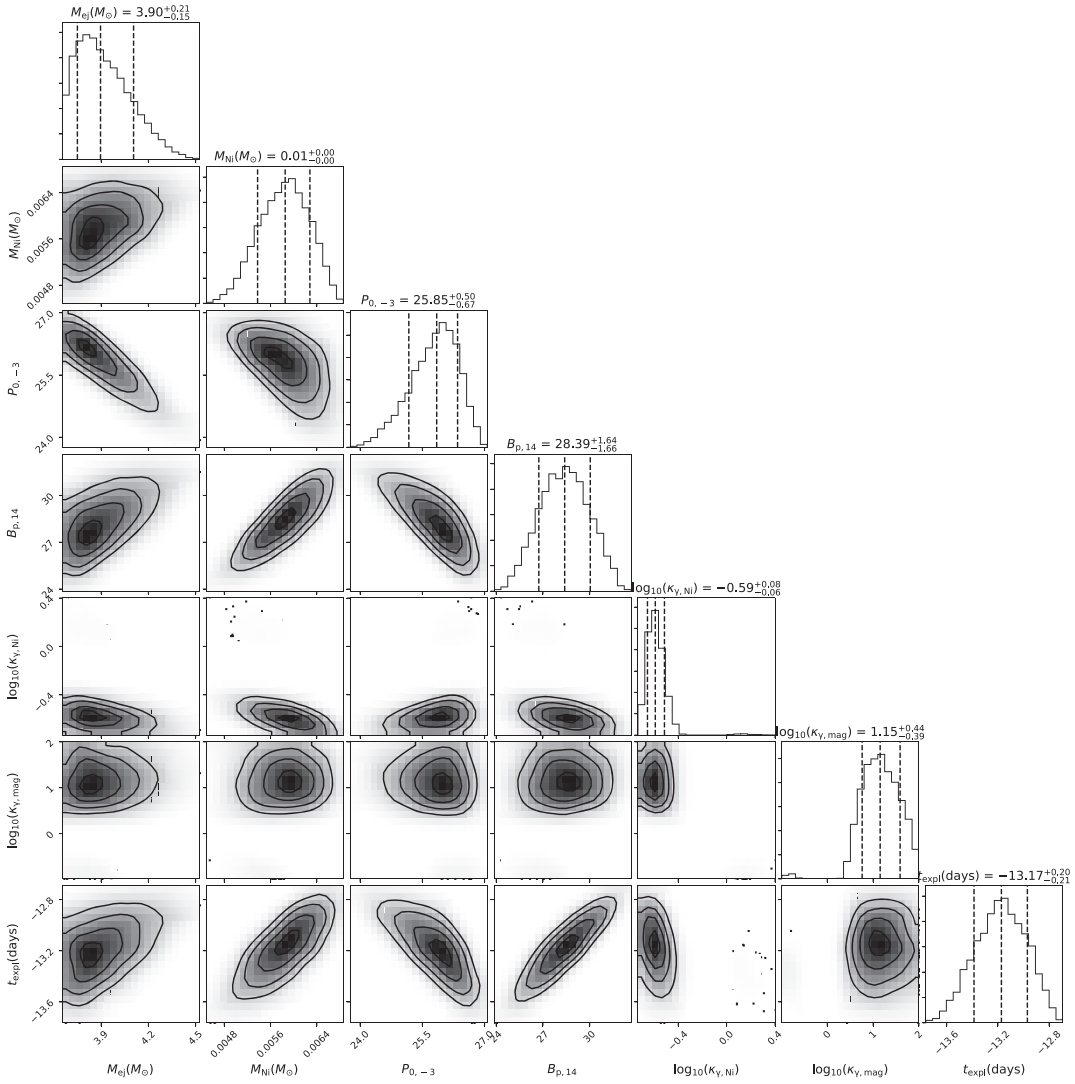

Figure 10. Corner plot of SN 2015ap showing the parameters (M_{ej}, M_{Ni}, P_0, B_p, $\kappa_{\gamma,Ni}$, $\kappa_{\gamma,mag}$, t_{expl}) of the ^{56}Ni + magnetar model.

as the [Ca II] lines may be contaminated with the [O II] 7320, 7330 Å (Fesen et al. 1999) lines and the Mg I] line is contaminated by Fe lines. Also, oxygen is the most abundant element in the SN ejecta and forms in a wavelength region where sensitivity of most of the spectrographs is maximum. The ratio of [O I] 6300/6364 Å lines changes from 1:1 to 3:1 for H-rich SNe when the density limit approaches 10^{10} cm^{-3} (Leibundgut et al. 1991; Pinto & Spyromilio 1991; Chugai 1992). While Taubenberger et al. (2009) suggested that during nebular phase, the ratio is always 3:1 for Type Ib SNe, Milisavljevic et al. (2010) argued that the ratio may be close to 1:1 in order to explain the dominance of double peaks in Type Ib rather than Type Ic. Maeda, Mazzali & Nomoto (2006) used a ratio of 3:1 for their nucleosynthesis models that was observationally confirmed by Hunter et al. (2009) for SN 2007gr. Maurer et al. (2010) showed that high-velocity Hα absorption feature can be superimposed on the oxygen emission profiles giving rise to double peaks.

SN 2015ap has a complex oxygen profile with multiple peaks/asymmetric shifted from 6300 Å as shown in Fig. 18(A). We do not detect any Hydrogen features in SN 2015ap, so the high-velocity feature as the reason for multipeaked profile is ruled out. The spectrum has been smoothed using a boxcar factor of 9 to reduce the noise. The signal-to-noise ratio (SNR) of all the peaks was checked in the smoothed spectrum of 124 d and compared with the background. The overall spectrum has a SNR of about 4. We checked the SNR of the individual peaks and found that the peak at -1600 km s^{-1} is of course real and is four times higher than the background, thus validating that the peak is real and hence confirming the existence of an asymmetric profile. The other peaks are two times higher than the background. As we obtain a blueshifted peak, we interpret this as per Taubenberger et al. (2009), which explains blueshift being originated due to either suppression of the redshifted part of the spectrum as dust forms or residual opacity as ejecta cools. These kinds of profiles have been seen previously in SNe 1990B, 1990aa, 1999dn, 2006F, and 2009jf (Taubenberger et al. 2009). Taubenberger et al. (2009) explained these asymmetric profiles that are produced by additional components of arbitrary widths and shifts with respect to main component. This indicates clumping of the SN ejecta on a large scale. It may also be due to a single massive blob and a unipolar jet. However, to check the evolution of line profiles, we check this in the three additional spectra taken from WISeREP (Yaron & Gal-Yam

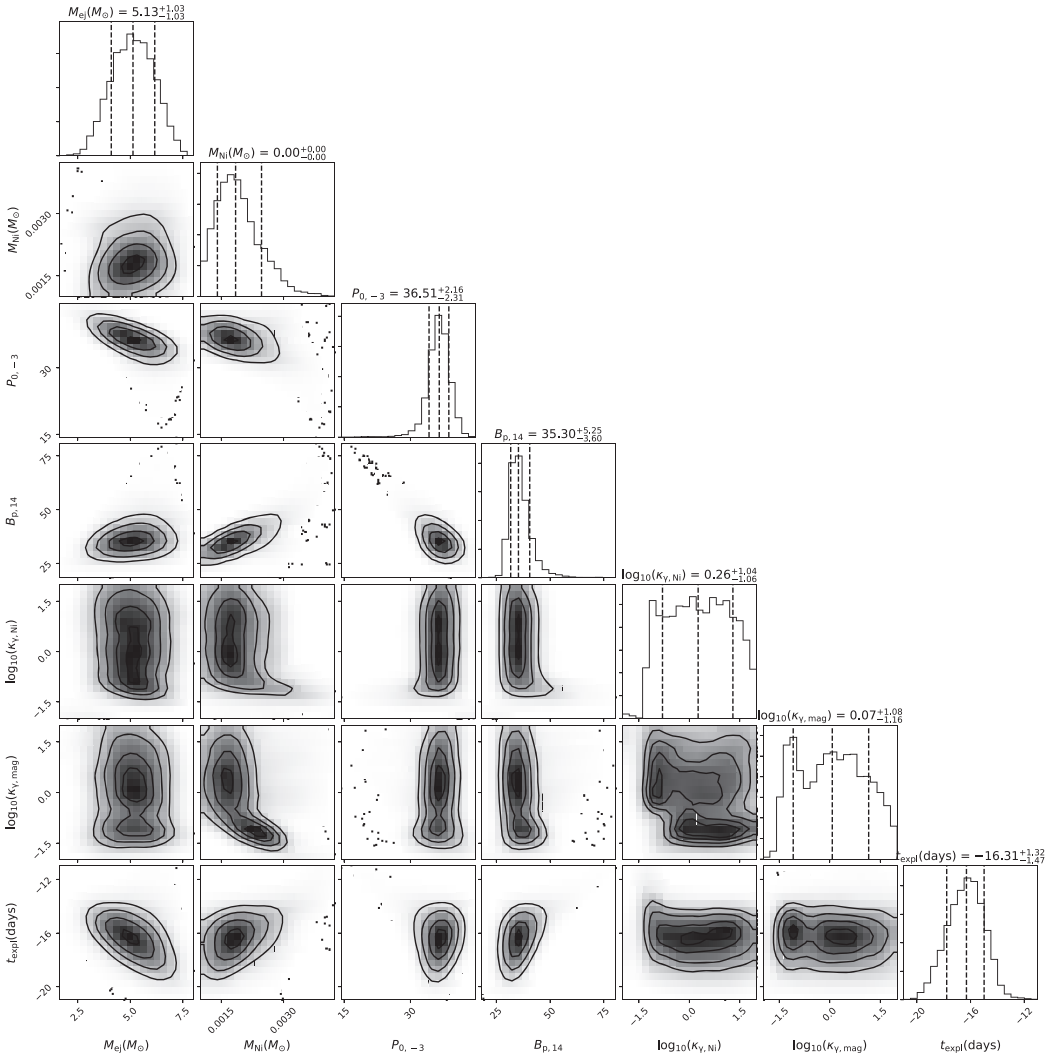

Figure 11. Corner plot of SN 2016P showing the parameters (M_{ej}, M_{Ni}, P_0, B_p, $\kappa_{\gamma,Ni}$, $\kappa_{\gamma,mag}$, t_{expl}) of the ^{56}Ni + magnetar model.

2012) public archive[3] and repeat the fitting procedure as discussed above. We find that the spectra of 124 and 125 d are well fitted with two Gaussians but the spectra of 128 and 144 d are well fitted with a single Gaussian (see Fig. 19). This indicates a transition in the [O I] line profile, but an overall clumpiness and asymmetric ejecta configuration are seen in all the profiles.

Fig. 18(A) also displays the Ca II profile. We see a blueshifted prominent peak in the doublet. This has a similar origin as that of [O I] profile (Taubenberger et al. 2009). The overall variation is, however, smooth as compared to the [O I] emission. Clumps of Ca do form, but they do not contribute significantly to emission. These clumps of Ca intercept gamma-ray radiation. However, as the mass fraction is small, the amount of radioactive luminosity and temperature achieved is not sufficient for the emission (Li, McCray & Sunyaev 1993; Matheson et al. 2000). The pre-existing envelope of the star is heated generally by hydrogen and helium that do not radiate efficiently, allowing Ca that was thoroughly mixed into the atmosphere, most likely present from the time of the progenitor formation, to reach the temperatures required to produce [Ca II] emission indicating a primordial origin.

Figs 18(B) and (C) compare the spectrum of SN 2015ap with a number of Type Ib/c SNe (phase range from 110 to 150 d) that are taken from WISeREP public archive. We see that the [O I] profile of SN 2015ap bears a resemblance with SNe 2007gt and 2009jf while [Ca II] profile bears a close resemblance with SN 2007hb. The [O I] profile of SN 2015ap shows a clumpy profile as compared to the double-peaked and single-peaked profiles of most of the other SNe. This may be due to the different geometrical orientation of the [O I] in different SN ejecta. If we look into the [Ca II] profiles, the profiles of all the Type Ib SNe have clumpiness less than the [O I] profiles. This may be due to the fact that the amount of primordial Calcium is more than the [Ca II] that are generated during the nucleosynthesis process going on in the SN evolution.

6.1 Estimates of the O mass and [O I]/[Ca II] ratio

The line strengths in the nebular phase spectra provide key information on the progenitor mass. Uomoto & Kirshner (1986) derived a relation, showing the minimum mass of O that can be estimated in

[3]https://wiserep.weizmann.ac.il

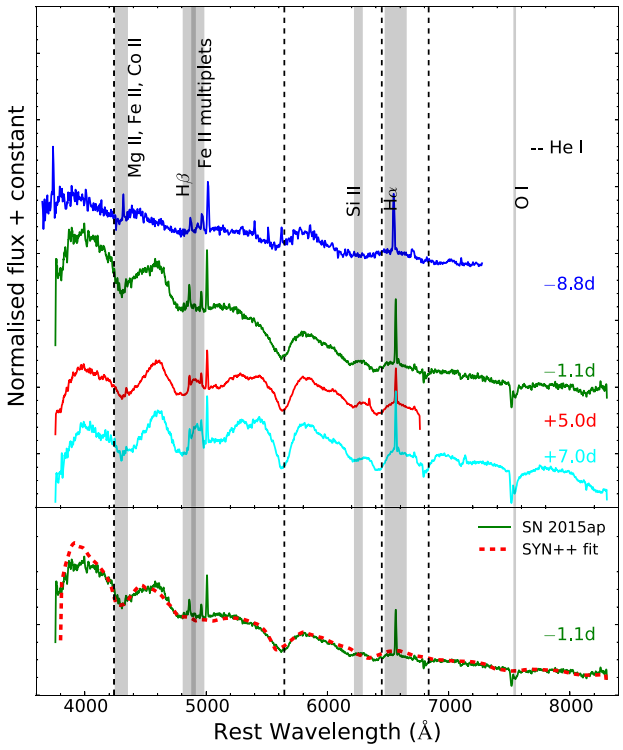

Figure 12. Early-time spectral evolution of SN 2015ap. Prominent He features are seen in early spectra. The bottom panel shows the −1.1 d spectrum plotted along with the best-fitting model generated by SYN++ (dotted lines). Prominent lines of He I are marked with vertical dashed black lines.

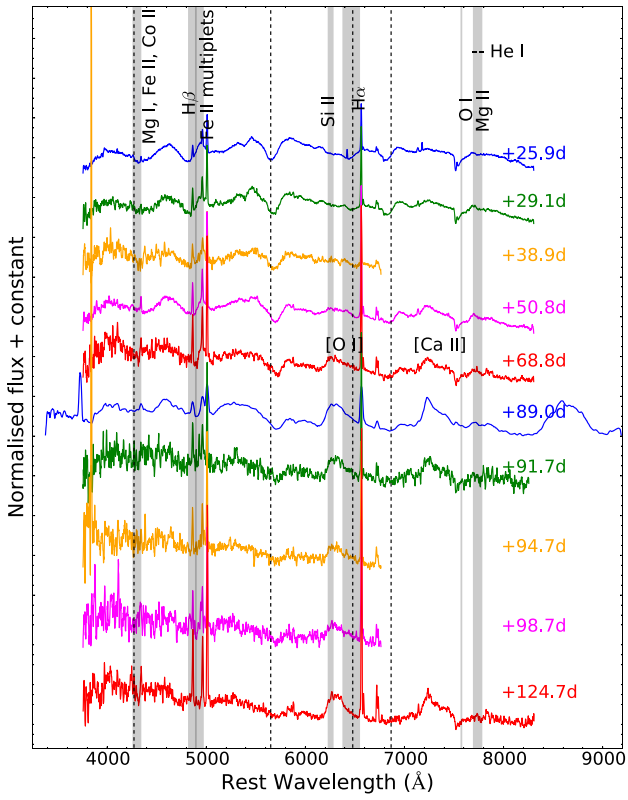

Figure 13. Spectral evolution of SN 2015ap between 25 to 124 d post *V*-maximum. Post 70 d, the [O I] and [Ca II] features start dominating.

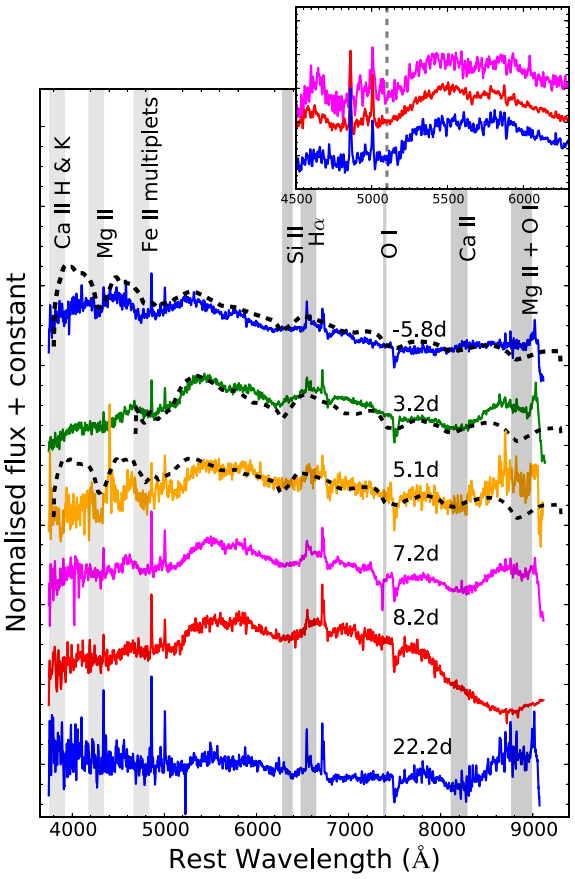

Figure 14. Spectral evolution of SN 2016P. The dotted lines in the first three spectra show the best-fitting SYN++ model. The shaded region at 5100 Å in the inset plot shows a shallow feature of unknown origin.

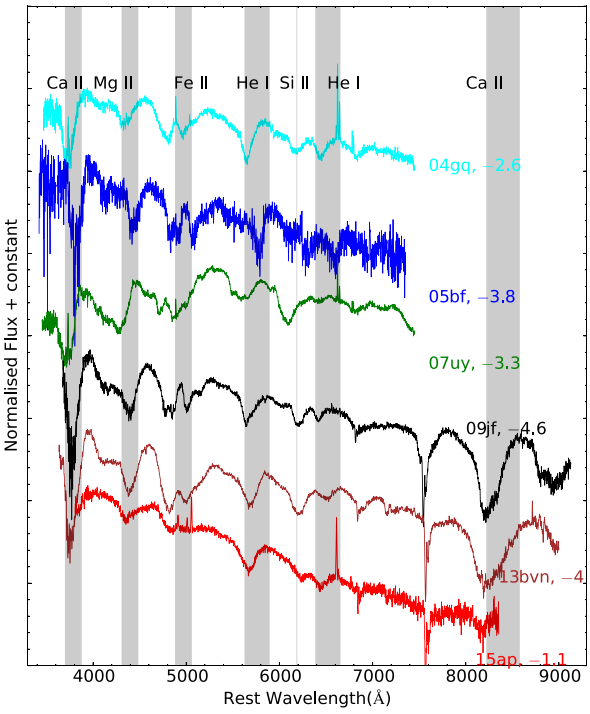

Figure 15. Spectral comparison of SN 2015ap along with other Type Ib SNe. SN 2015ap shows a distinct blue continuum.

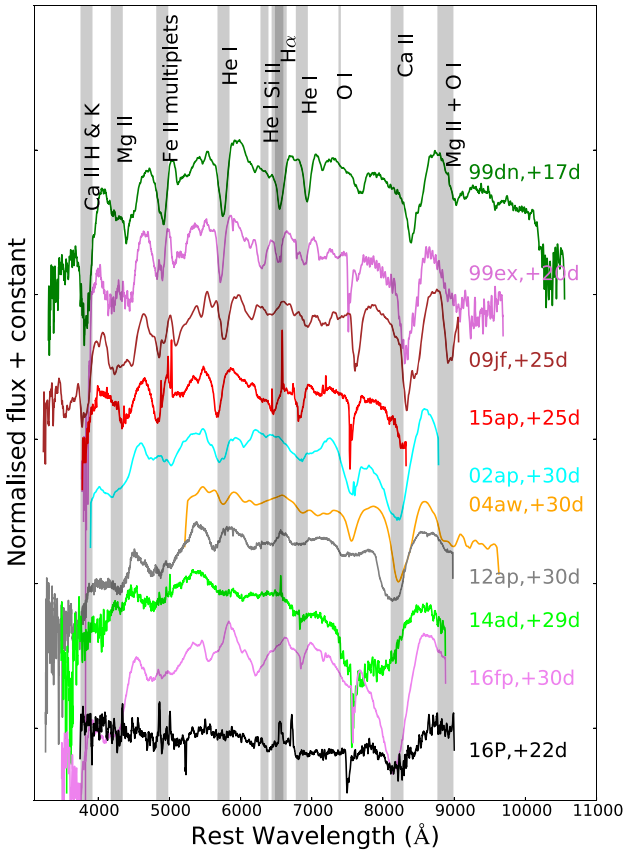

Figure 16. Spectral comparison of SNe 2015ap and 2016P at ∼25 d post *V*-maximum with other SNe. The overall spectrum of SNe 2015ap and 2016P shows resemblance with SNe 2009jf and 2012ap, respectively.

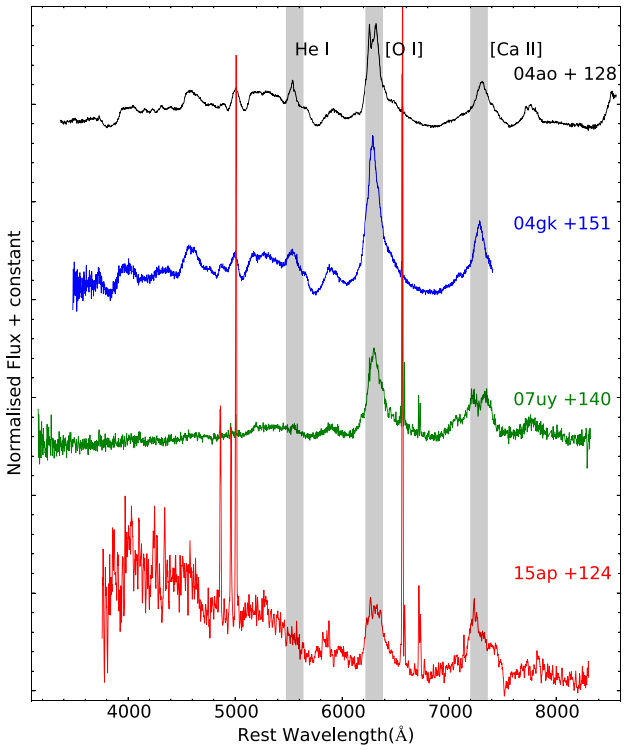

Figure 17. Nebular phase comparison of SN 2015ap shows less prominent emission peaks than other SNe. SN 2015ap shows distinct multipeaked profiles of [O I] different from all other SNe.

the high density ($N_e \geq 10^6$ cm^{-3}) limit (Schlegel & Kirshner 1989; Elmhamdi et al. 2004). This is given by

$$M_O = 10^8 \times D^2 \times F([O\,I]) \times \exp^{(2.28/T_4)}, \quad (3)$$

where M_O is the mass of the neutral O in M$_\odot$ units, D is distance to the galaxy in Mpc, F([O I]) is the total flux of the [O I] 6300, 6364 Å feature in erg s^{-1} cm^{-2}, and T_4 is the temperature of the O-emitting region in units of 10^4 K. Ideally, the ratio of [O I] 5577 Å to the [O I] 6300, 6364 Å feature should be considered. Osterbrock (1989) showed that the ratio of [O I] 5577 Å to [O I] 6300 is proportional to the electron density and the temperature of the emitting regions. Thus, the uncertainties associated in the equation are large, which involves the errors due to the flux, temperature, and indirectly the density. The temperatures can typically vary between (0.4–1) × 10^4 K. We find that the [O I] 5577 Å line is very faint, and the limit of the flux ratio is ≤0.1. Using the observed flux of 3.0 × 10^{-14} erg s^{-1} cm^{-2} of the [O I] 6300, 6364 Å doublet from the 2016 January 22 spectrum, and adopting $T_4 = 0.4$ K, we estimate M_O = 0.90 M$_\odot$. A very weak O I 7774 Å emission feature is seen in the nebular spectra. Since the O I 7774 line is expected to result from recombination of ionized O (Begelman & Sarazin 1986), the O mass required to produce the [O I] doublet and the O I 7774 Å line is higher than the mass required to produce the doublet alone (Mazzali et al. 2010). Therefore, 0.90 M$_\odot$ can be considered as a lower limit of total oxygen mass ejected in the explosion. [O I] layer is mostly produced by hydrostatic burning of oxygen. Thielemann, Nomoto & Hashimoto (1996) made explosive nucleosynthesis calculations and predicted major nucleosynthesis yields for the progenitor mass of 13–25 M$_\odot$. For progenitor masses of 13, 15, 20, and 25 M$_\odot$, Thielemann et al. (1996) showed that the corresponding O masses would be 0.22, 0.43, 1.48, and 3.0 M$_\odot$, respectively. Also, Thielemann et al. (1996) estimated He core masses of 3.3, 4, and 8 M$_\odot$, corresponding to progenitors of 13, 15, and 25 M$_\odot$, respectively. Thus, using this model and corresponding approximations, we conclude that the progenitor of SN 2015ap is most likely a star between 15 and 20 M$_\odot$ and He core mass between 4 and 8 M$_\odot$.

Kuncarayakti et al. (2015) estimated the value of [O I]/[Ca II] ratio for a group of CCSNe and found that this ratio is highly dependent on temperature, density, and progenitor mass. Kuncarayakti et al. (2015) considered a demarcation of SN progenitors as binary and single if this ratio was lower or higher than 1.5, respectively. However, this ratio is close to 0.7 for Type IIP SNe. In the case of SN 2015ap, the [O I]/[Ca II] ratio is ∼0.71, indicating that the progenitor is a low-mass star in a binary system.

6.2 Progenitor mass from oxygen line luminosities

The observed strength of the nebular lines can serve as an important diagnostic of the progenitor mass. Jerkstrand et al. (2012, 2014) generated nucleosynthesis models for progenitor masses of 12, 15, 19, and 25 M$_\odot$, assuming ^{56}Ni mass to be 0.062 M$_\odot$ and distance of 5.5 Mpc for a group of Type IIP SNe. Jerkstrand et al. (2015) extended this for a group of SE-SNe by implementing minor modifications in the code. They generated three models of 12, 13, and 17 M$_\odot$ for the stripped envelope group with ^{56}Ni mass = 0.079 M$_\odot$ and distance of 7.9 Mpc. In Fig. 20, we compare the 137 d post-explosion (or 124 d since *V*-maximum) spectrum of SN 2015ap with the 150 d and 12, 13, and 17 M$_\odot$ model generated by Jerkstrand et al. (2015) for Type IIb/Ib

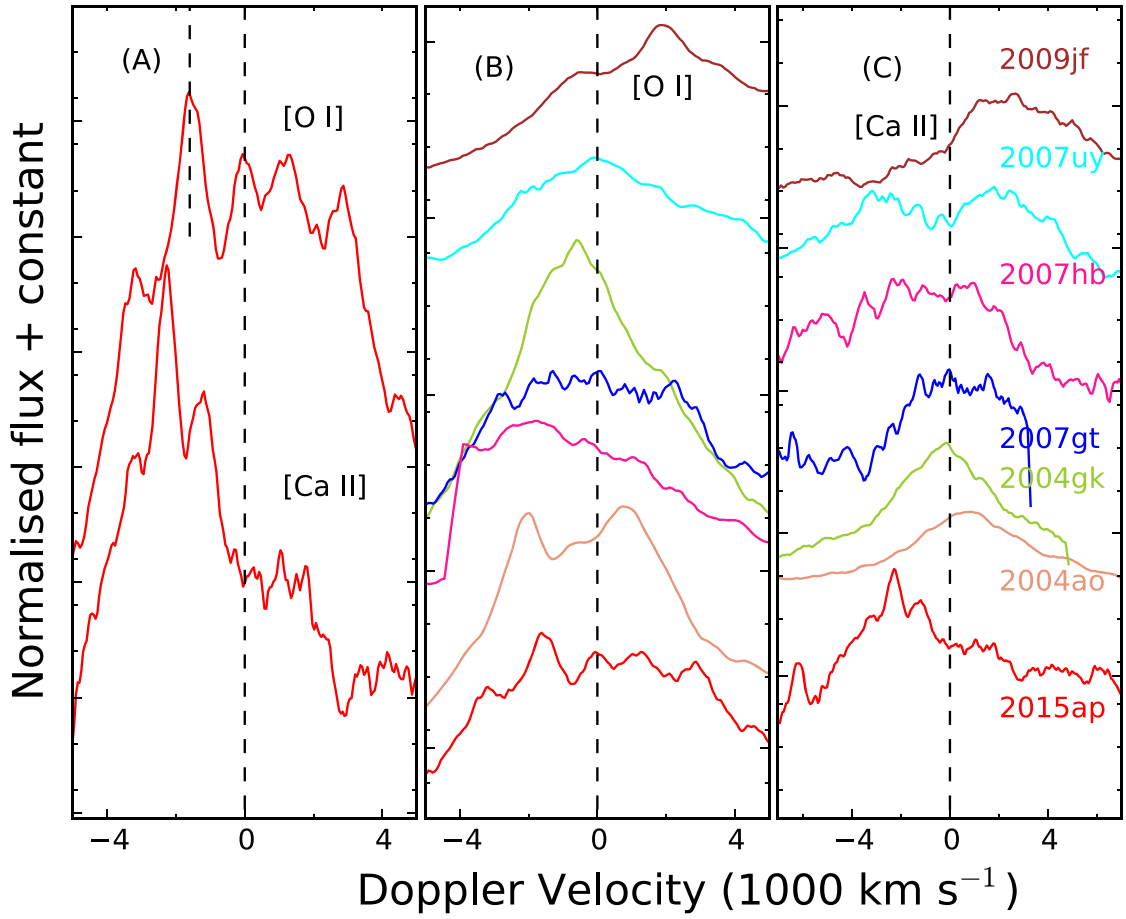

Figure 18. Panel (A) of the figure represents the line profiles of [O I] 6300, 6364 Å and [Ca II] 7291, 7324 Å. Panels (B) and (C) show the comparison of the [O I] and [Ca II] profile of SNe 2015ap with other Type Ib/c SN sample. The black dashed lines in Fig. 18 (A) represent the zero velocity line corresponding to 6300 Å and left line represents the real peak at −1600 km s^{-1}. In panel (B), the black line represents the velocity corresponding to 6300 Å and panel (C) represents the velocity corresponding to 7291 Å line.

SNe. It is to be noted that the model assumes elemental abundances that are higher than the estimates of lower progenitor mass.

We modelled the spectra of SN 2015ap adopting a ratio of (0.26/0.079) to correct ^{56}Ni mass and rescale the model flux (150 d) to the distance and phase of the (137 d) nebular spectrum of SN 2015ap. The SN spectrum is de-reddened and de-redshifted to avoid any flux loss before comparison. We see that the overall spectrum matches better with a 12 $M_{\odot}$ progenitor star. We then, subtracted the host galaxy spectrum taken from SDSS DR14 of SN 2015ap from the SN spectrum. Fig. 20 shows both the subtracted and unsubtracted spectrum of SN 2015ap. The galaxy lines of H and S II are removed in this spectrum and also there is an overall flux decrement, implying a progenitor of mass less than 12 $M_{\odot}$. It is to remark, however, that these models assume an overabundance of elements as compared with Thielemann et al. (1996), so a lower progenitor mass would indicate an overestimated peak. Also, due to the high-density envelope used in the model, scattering of other lines may affect the flux estimations. The [O I] feature matches well with a 12 $M_{\odot}$ progenitor star for the unsubtracted spectrum. Our obtained value of $L_{\rm norm} = 0.015$ that is a good tracer of $L_{\rm [O\,I]}$ (Jerkstrand et al. 2015) matches well with the value estimated by Prentice et al. (2019). Comparing the line luminosities of [O I] and the fitted nebular spectral modelling indicates that the progenitor of SN 2015ap is in the range of 12–20 $M_{\odot}$, which is most likely in a binary association.

6.3 Host galaxy metallicity

Metallicity is a key parameter driving mass-loss rates in single stars and influences the relative number of Type Ib/c SNe. It is also important for binary models (Eldridge et al. 2008) and affects the ratios of Type Ib/c SNe. In order to estimate the host galaxy metallicity, we used the Sloan Digital Sky Survey (SDSS) spectrum of IC 1776, the host galaxy of SN 2015ap. The DR12 SDSS image was taken on 2010 November 13.[4] Narrow emission lines of [O III] 5007 Å and the [N II] 6583 Å lines are clearly visible in the host galaxy spectrum. Several diagnostics are used to estimate the host galaxy metallicity (McGaugh 1991; Kewley & Dopita 2002; Pettini & Pagel 2004; Pilyugin & Thuan 2005). We used the O3N2 index calibration given by Pettini & Pagel (2004) to estimate the host galaxy metallicity. The value of 12 + log(O/H) is found to be 8.8 ± 0.6 dex. For SN 2016P, the SDSS DR12 image of the galaxy NGC 5374 was taken on 2007 March 16.[5] In this spectrum also, narrow emission lines of [O III] 5007 Å and the [N II] 6583 Å were seen. The value of 12 + log(O/H) for NGC 5374 is found to be 8.7 ± 0.5 dex.

[4] https://dr12.sdss.org/spectrumDetail?mjd=55514&fiber=999&plateid=4402

[5] https://dr12.sdss.org/spectrumDetail?mjd=54176&fiber=301&plateid=1808

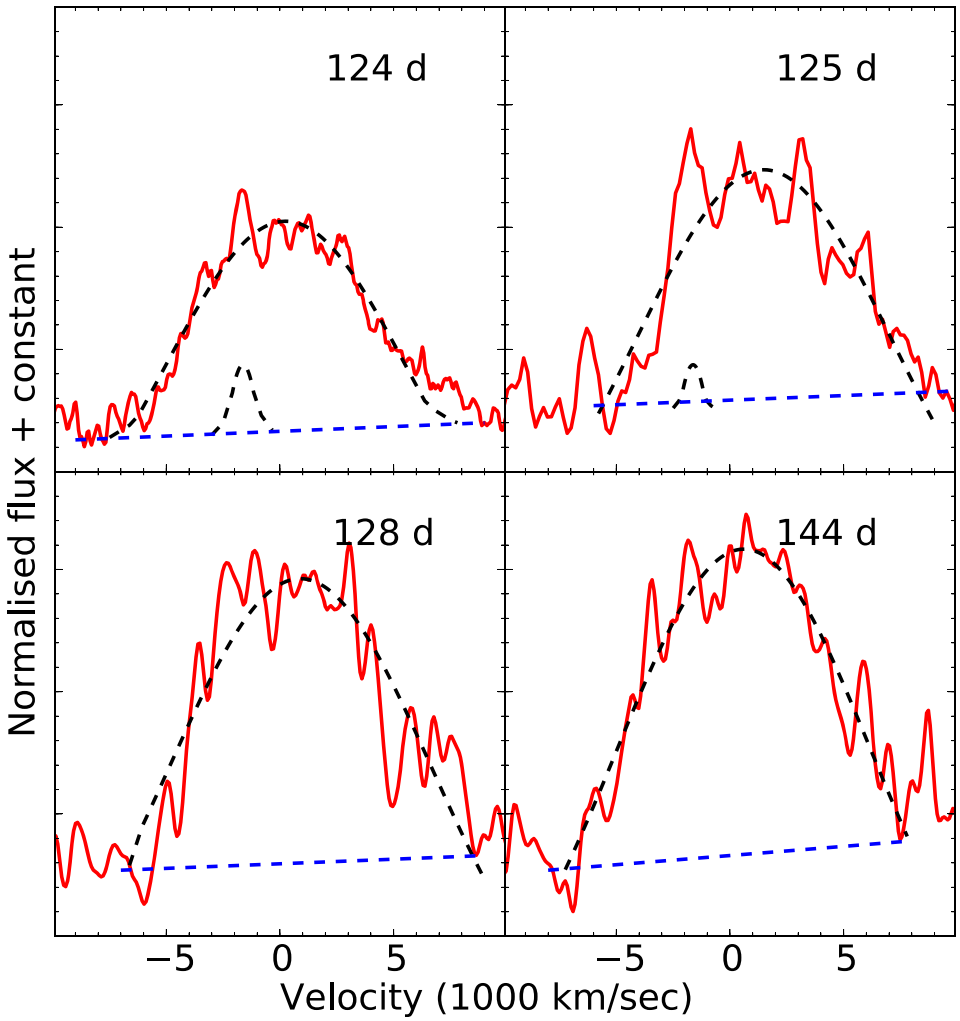

Figure 19. Oxygen profile of SN 2015ap fitted with Gaussian profiles. The top two panels show two peaks while the bottom two panels show an overall asymmetric structure.

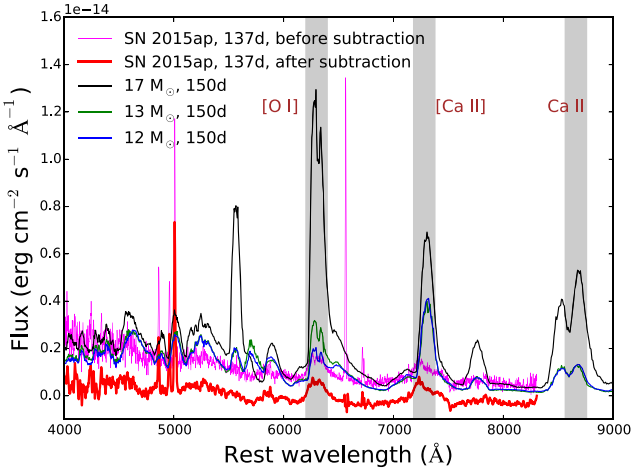

Figure 20. The 137 d since explosion spectrum of SN 2015ap plotted along with the 12, 13, and 17 $M_{\odot}$ models of Jerkstand et al. (2015) at 150 d. The 12 $M_{\odot}$ model best matches our observed spectrum of SN 2015ap.

Several authors have estimated the solar metallicity values to be 8.69 ± 0.05, 8.69, and 8.76 ± 0.07 dex (Allende Prieto et al. 2001; Asplund et al. 2009; Caffau et al. 2011). The obtained metallicity value for IC 1776 is slightly supersolar while NGC 5374 has nearly solar metallicity. However, the metallicity is close to solar for both the galaxies within errors. Wolf–Rayet (WR) progenitor could be one of the favourable scenarios as the number of WR stars increases with increasing metallicity due to the strong metallicity dependence on stellar winds (Vink & de Koter 2005; López-Sánchez & Esteban 2010). The progenitors could be in the form of either single WR stars or in binary association. Galbany et al. (2016) estimated the metallicity of a group of Type II and Ib/c SNe and found an average metallicity of 8.50 dex with an error of 0.02 for all SNe. Their results support a binary progenitor for SNe Ib and at least a fraction of SNe Ic to be single massive stars that have stripped their outer layers by metallicity-driven winds.

7 SUMMARY

In this paper, we present the temporal and spectral evolution of a Type Ib SN 2015ap and a Type Ic SN 2016P. The early decline rates

of SNe 2015ap and 2016P are consistent with other Type Ib/c SNe while the late-time light curves of both the SNe show steepening. The colours of SN 2015ap are similar to most Type Ib comparison sample while the colour evolution of SN 2016P is redder than most of the members. The absolute magnitude ($M_V = -18.04 \pm 0.19$ mag) of SN 2015ap indicates that it lies at the brighter end of Type Ib SN among the comparison sample while SN 2016P lies in the middle ($M_V = -17.53 \pm 0.14$ mag) among Type Ic sample. The bolometric light-curve modelling of SNe 2015ap and 2016P indicates that the light curves can be best fitted by a ^{56}Ni + magnetar model with ^{56}Ni masses of 0.01 and 0.002 $M_\odot$, ejecta masses of 3.75 and 4.66 $M_\odot$, spin period P_0 of 25.8 and 36.5 ms, and magnetic field B_p of 28.39×10^{14} and 35.3×10^{14} G, respectively. We suspected an additional energy source from a newly born magnetar because of the inability to fit the late-time light curves and high luminosity. The narrow light curve and short rise time for SN 2015ap implied that the high ejecta mass is most likely a resultant of terminal fallback.

Early-time spectral sequence of SN 2015ap shows prominent He I absorption lines with a blue continuum and high photospheric temperature. SYN++ modelling of the early-time spectra of SN 2015ap indicates a photospheric temperature of 13 000 K and a photospheric velocity of 16 000 km s^{-1}. Initial spectral sequence shows a 'W'-like feature arising due to Fe complexes. SN 2016P shows prominent lines of Ca II H&K, Mg II, Fe II, and Ca II NIR features. The broad absorption blueward of 6000 Å mostly arises due to a blend of Si II and C II. SYN++ modelling gives an initial photospheric velocity of $v_{ph} = 15\,000$ km s^{-1} and a temperature of 8000 K.

The [O I] profile of SN 2015ap shows an asymmetric profile that is indicative of large-scale clumping or a unipolar jet. The [O I] and [Ca II] doublet shows blueshifted peak originating from residual opacity or dust formation. [Ca II] envelope has an origin of pre-SN envelope. The estimated O mass is found to be 0.90 $M_\odot$. The [O I]/[Ca II] ratio and the Jerkstrand modelling indicate a progenitor of mass between 12 and 20 $M_\odot$ and most likely in binary association (Sana, James & Gosset 2011).

ACKNOWLEDGEMENTS

We sincerely thank the referee for his/her valuable comments and input that have improved the presentation of the paper. We thank the observing staff and observing assistants at 1.04 m ST, 1.30 m DFOT, 1.82 m EKAR Asiago Telescope, and 2.00 m HCT for their support during observations. We thank Andrea Pastorello for coordinating the observation of SN 2015ap with Asiago Telescope. We acknowledge Wiezmann Interactive Supernova data REPository http://wiserep.weizmann.ac.il (WISeREP). BK acknowledges the Science and Engineering Research Board (SERB) under the Department of Science & Technology, Government of India, for financial assistance in the form of National Post-Doctoral Fellowship (Ref. no. PDF/2016/001563). LT is partially supported by the 'PRIN-INAF 2017' with the project 'Towards the SKA and CTA era: discovery, localization, and physics of transient objects'. The work made use of the *Swift* Optical/Ultraviolet Supernova Archive (SOUSA). SOUSA is supported by NASA's Astrophysics Data Analysis Program through grant NNX13AF35G. SBP and KM acknowledge BRICS grant DST/IMRCD/BRICS/Pilotcall/ProFCheap/2017(G) for this work. NER acknowledges support from the Spanish MICINN grant ESP2017-82674-R and FEDER funds.

DATA AVAILABILITY

The data underlying this article will be shared on reasonable request to the corresponding author.

REFERENCES

Allende Prieto C., Barklem P. S., Asplund M., Ruiz Cobo B., 2001, ApJ, 558, 830
Arnett W. D., 1982, ApJ, 253, 785
Asplund M., Grevesse N., Sauval A. J., Scott P., 2009, ARA&A, 47, 481
Begelman M. C., Sarazin C. L., 1986, ApJ, 302, L59
Benetti S. et al., 2011, MNRAS, 411, 2726
Bersten M. C. et al., 2014, AJ, 148, 68
Bianco F. B. et al., 2014, ApJS, 213, 19
Brown P. J., Breeveld A. A., Holland S., Kuin P., Pritchard T., 2014, Ap&SS, 354, 89
Caffau E., Ludwig H.-G., Steffen M., Freytag B., Bonifacio P., 2011, Sol. Phys., 268, 255
Cano Z., 2013, MNRAS, 434, 1098
Cano Z., Maeda K., Schulze S., 2014, MNRAS, 438, 2924
Cao Y. et al., 2013, ApJ, 775, L7
Chatzopoulos E., Wheeler J. C., Vinko J., 2012, ApJ, 746, 121
Chugai N. N., 1992, Sov. Astron. Lett., 18, 239
Clocchiatti A., Wheeler J. C., 1997, ApJ, 491, 375
Dessart L., Hillier D. J., Li C., Woosley S., 2012, MNRAS, 424, 2139
Dessart L., Hillier D. J., Woosley S., Livne E., Waldman R., Yoon S.-C., Langer N., 2016, MNRAS, 458, 1618
Drout M. R. et al., 2011, ApJ, 741, 97
Drout M. R. et al., 2016, ApJ, 821, 57
Eldridge J. J., Maund J. R., 2016, MNRAS, 461, L117
Eldridge J. J., Izzard R. G., Tout C. A., 2008, MNRAS, 384, 1109
Elmhamdi A., Danziger I. J., Cappellaro E., Della Valle M., Gouiffes C., Phillips M. M., Turatto M., 2004, A&A, 426, 963
Fesen R. A. et al., 1999, AJ, 117, 725
Filippenko A. V., 1997, ARA&A, 35, 309
Folatelli G. et al., 2016, ApJ, 825, L22
Foley R. J. et al., 2003, PASP, 115, 1220
Fremling C. et al., 2014, A&A, 565, A114
Fremling C. et al., 2016, A&A, 593, A68
Galama T. J. et al., 1999, A&AS, 138, 465
Galbany L. et al., 2016, A&A, 591, A48
Galbany L. et al., 2018, ApJ, 855, 107
Gangopadhyay A. et al., 2018, MNRAS, 476, 3611
Gehrels N., 2004a, APS Meeting Abstracts, #S10.001
Gehrels N., 2004b, in Fenimore E., Galassi M., eds, AIP Conf. Proc. Vol. 727, Gamma-Ray Bursts: 30 Years of Discovery. Am. Inst. Phys., New York, p. 637
Groh J. H., Georgy C., Ekström S., 2013, A&A, 558, L1
Harutyunyan A. H. et al., 2008, A&A, 488, 383
Heger A., Fryer C. L., Woosley S. E., Langer N., Hartmann D. H., 2003, ApJ, 591, 288
Hirai R., 2017a, MNRAS, 466, 3775
Hirai R., 2017b, MNRAS, 469, L94
Hunter D. J. et al., 2009, A&A, 508, 371
Inserra C. et al., 2013, ApJ, 770, 128
Jerkstrand A., Fransson C., Maguire K., Smartt S., Ergon M., Spyromilio J., 2012, A&A, 546, A28
Jerkstrand A., Smartt S. J., Fraser M., Fransson C., Sollerman J., Taddia F., Kotak R., 2014, MNRAS, 439, 3694
Jerkstrand A., Ergon M., Smartt S. J., Fransson C., Sollerman J., Taubenberger S., Bersten M., Spyromilio J., 2015, A&A, 573, A12
Jordi K., Grebel E. K., Ammon K., 2006, A&A, 460, 339
Kewley L. J., Dopita M. A., 2002, ApJS, 142, 35
Kilpatrick C. D. et al., 2018, MNRAS, 480, 2072
Kumar B., Singh A., Srivastav S., Sahu D. K., Anupama G. C., 2018, MNRAS, 473, 3776
Kuncarayakti H. et al., 2015, A&A, 579, A95

Leibundgut B., Kirshner R. P., Pinto P. A., Rupen M. P., Smith R. C., Gunn J. E., Schneider D. P., 1991, ApJ, 372, 531
Li H., McCray R., Sunyaev R. A., 1993, ApJ, 419, 824
López-Sánchez Á. R., Esteban C., 2010, A&A, 516, A104
Lyman J. D., Bersier D., James P. A., Mazzali P. A., Eldridge J. J., Fraser M., Pian E., 2016, MNRAS, 457, 328
Maeda K., Mazzali P. A., Nomoto K., 2006, ApJ, 645, 1331
Maeda K. et al., 2008, Science, 319, 1220
Matheson T., 2001, PASP, 113, 1155
Matheson T. et al., 2000, AJ, 120, 1487
Maurer I., Mazzali P. A., Taubenberger S., Hachinger S., 2010, MNRAS, 409, 1441
Mazzali P. A. et al., 2005, Science, 308, 1284
Mazzali P. A. et al., 2008, Science, 321, 1185
Mazzali P. A., Maurer I., Valenti S., Kotak R., Hunter D., 2010, MNRAS, 408, 87
McGaugh S. S., 1991, ApJ, 380, 140
Milisavljevic D., Fesen R. A., Gerardy C. L., Kirshner R. P., Challis P., 2010, ApJ, 709, 1343
Modjaz M. et al., 2006, ApJ, 645, L21
Modjaz M., Kirshner R. P., Blondin S., Challis P., Matheson T., 2008, ApJ, 687, L9
Modjaz M. et al., 2009, ApJ, 702, 226
Modjaz M., Liu Y. Q., Bianco F. B., Graur O., 2016, ApJ, 832, 108
Nomoto K., Kobayashi C., Tominaga N., 2013, ARA&A, 51, 457
Osterbrock D. E., 1989, Sky Telesc., 78, 491
Pandey S. B., Anupama G. C., Sagar R., Bhattacharya D., Castro-Tirado A. J., Sahu D. K., Parihar P., Prabhu T. P., 2003, A&A, 408, L21
Pettini M., Pagel B. E. J., 2004, MNRAS, 348, L59
Pignata G. et al., 2011, ApJ, 728, 14
Pilyugin L. S., Thuan T. X., 2005, ApJ, 631, 231
Pinto P. A., Spyromilio J., 1991, Bull. Am. Astron. Soc., 23, 881
Podsiadlowski P., Joss P. C., Hsu J. J. L., 1992, ApJ, 391, 246
Prentice S. J. et al., 2016, MNRAS, 458, 2973
Prentice S. J. et al., 2019, MNRAS, 485, 1559
Pritchard T. A., Roming P. W. A., Brown P. J., Bayless A. J., Frey L. H., 2014, ApJ, 787, 157
Puls J., Vink J. S., Najarro F., 2008, A&AR, 16, 209
Quimby R. M., Aldering G., Wheeler J. C., Höflich P., Akerlof C. W., Rykoff E. S., 2007, ApJ, 668, L99
Richardson D., Branch D., Baron E., 2006, AJ, 131, 2233
Richmond M. W. et al., 1996, AJ, 111, 327
Roming P. W. A. et al., 2005, Space Sci. Rev., 120, 95
Sahu D. K., Tanaka M., Anupama G. C., Gurugubelli U. K., Nomoto K., 2009, ApJ, 697, 676
Sahu D. K., Gurugubelli U. K., Anupama G. C., Nomoto K., 2011, MNRAS, 413, 2583
Sahu D. K., Anupama G. C., Chakradhari N. K., Srivastav S., Tanaka M., Maeda K., Nomoto K., 2018, MNRAS, 475, 2591
Sana H., James G., Gosset E., 2011, MNRAS, 416, 817
Schlafly E. F., Finkbeiner D. P., 2011, ApJ, 737, 103
Schlegel E. M., Kirshner R. P., 1989, AJ, 98, 577
Shivvers I., Yuk H., Zheng W., Filippenko A. V., 2015, Astron. Telegram, 8081
Shivvers I. et al., 2017, MNRAS, 471, 4381
Silverman J. M., Mazzali P., Chornock R., Filippenko A. V., Clocchiatti A., Phillips M. M., Ganeshalingam M., Foley R. J., 2009, PASP, 121, 689
Smartt S. J., 2009, ARA&A, 47, 63
Smith N., Owocki S. P., 2006, ApJ, 645, L45
Srivastav S., Anupama G. C., Sahu D. K., 2014, MNRAS, 445, 1932
Stalin C. S., Hegde M., Sahu D. K., Parihar P. S., Anupama G. C., Bhatt B. C., Prabhu T. P., 2008, Bull. Astron. Soc. India, 36, 111
Stetson P. B., 1992, J. R. Astron. Soc. Canada, 86, 71
Taddia F. et al., 2015, A&A, 574, A60
Taddia F. et al., 2018, A&A, 609, A136
Tartaglia L. et al., 2015, Astron. Telegram, 8039
Taubenberger S. et al., 2006, MNRAS, 371, 1459
Taubenberger S. et al., 2009, MNRAS, 397, 677
Thielemann F.-K., Nomoto K., Hashimoto M.-A., 1996, ApJ, 460, 408
Thomas R. C., Nugent P. E., Meza J. C., 2011, PASP, 123, 237
Uomoto A., Kirshner R. P., 1986, ApJ, 308, 685
Valenti S. et al., 2008a, MNRAS, 383, 1485
Valenti S. et al., 2008b, ApJ, 673, L155
Valenti S. et al., 2011, MNRAS, 416, 3138
Van Dyk S. D. et al., 2018, ApJ, 860, 90
Vink J. S., de Koter A., 2005, A&A, 442, 587
Wang S. Q., Wang L. J., Dai Z. G., Wu X. F., 2015a, ApJ, 799, 107
Wang S. Q., Wang L. J., Dai Z. G., Wu X. F., 2015b, ApJ, 807, 147
Wheeler J. C., Levreault R., 1985, ApJ, 294, L17
Woosley S. E., Weaver T. A., 1986, Bull. Am. Astron. Soc., 18, 1016
Woosley S. E., Langer N., Weaver T. A., 1995, ApJ, 448, 315
Yaron O., Gal-Yam A., 2012, PASP, 124, 668
Yoon S.-C., Woosley S. E., Langer N., 2010, ApJ, 725, 940
Yoshii Y. et al., 2003, ApJ, 592, 467
Zhang J., Wang X., 2016, Astron. Telegram, 8563

SUPPORTING INFORMATION

Supplementary data are available at *MNRAS* online.

Table A1. Star ID and the magnitudes in UBVRI filters of the five secondary standards in the field of SN 2015ap.
Table A2. Star ID and the magnitudes in BVRI filters of the six secondary standards in the field of SN 2016P.
Table A5. Log of spectroscopic observations of SN 2015ap.
Table A6. Log of spectroscopic observation of SN 2016P.

Please note: Oxford University Press is not responsible for the content or functionality of any supporting materials supplied by the authors. Any queries (other than missing material) should be directed to the corresponding author for the article.

APPENDIX: PHOTOMETRY

In addition to the ground-based telescopes, SN 2015ap was observed with *Swift* UVOT (Gehrels 2004a, b; Roming et al. 2005) from 2015 September 9 to 2015 October 6. We take the *Swift* early *UBV* magnitudes from the *Swift* Optical/Ultraviolet Supernova Archive (SOUSA; Brown et al. 2014) and tabulate them in Table A3.

The SN instrumental magnitudes were calibrated with respect to the local standards in the SN field. Three Landolt standard fields PG 2331, PG 0918, and PG 0231 were observed along with the SN fields with HFOSC/HCT to generate a sequence of local standards. The observations were carried out at different altitudes with airmass varying between 1.1 and 2.0 with a typical seeing of $\leq$2 arcsec in the *V* band. The instrumental and catalogue magnitudes of Landolt field stars were fitted, using the least-squares regression technique, to estimate the zero-points and colour term using a set of transformation equations (Stetson 1992). Site extinction values, taken from Stalin et al. (2008), were used for the different filters. A root-mean-squared scatter between transformed and standard magnitude of Landolt stars was found to be between 0.02 and 0.05 mag in the *UBVRI* bands. Using the above zero-points and colour term, we calibrated the magnitudes of 5–6 non-variable local standards in both the SN fields (Tables A1 and A2, available online). These secondary standards are used to calibrate the SN instrumental magnitudes by applying nightly zero-points. The errors due to calibration and photometric measurement were added in quadrature to estimate the final error on the SN magnitudes. Wherever required, the *uri* magnitudes were converted to *URI* using the equations of Jordi, Grebel & Ammon (2006). The final photometry of SNe 2015ap and 2016P is given in Tables A3 and A4, respectively.

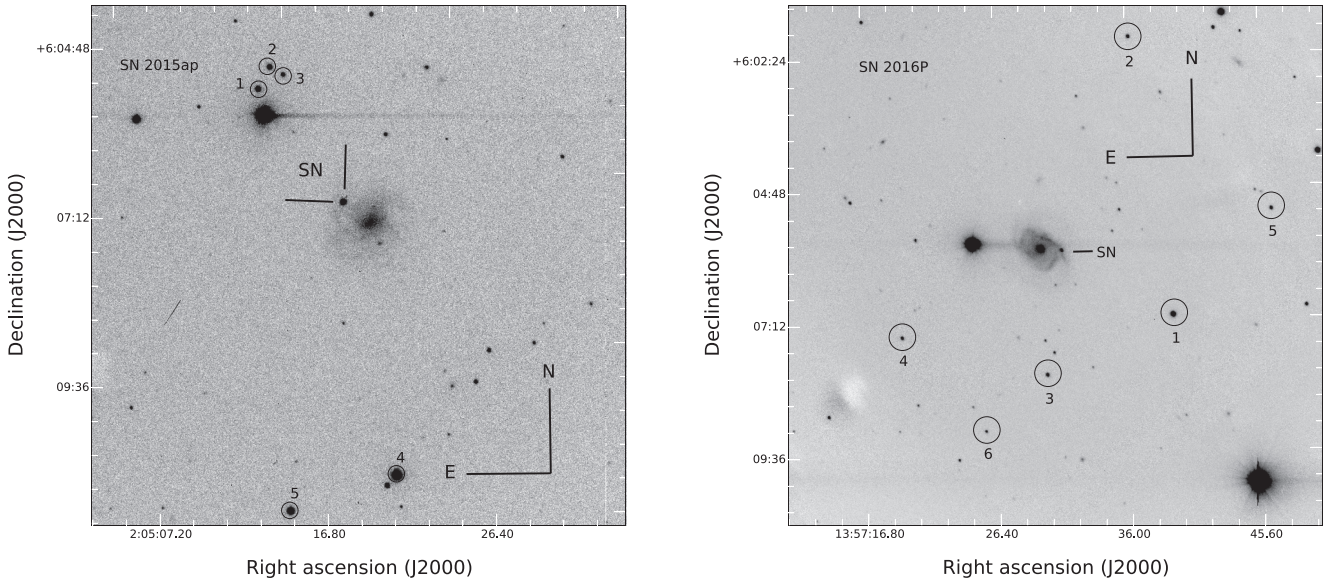

Figure A1. SNe 2015ap and 2016P and the local standard stars in the field of IC 1776 and NGC 5374, and *R*-band, 300 s image obtained on 2015 September 26 and 2016 January 23 with the 2.0 m HCT for SNe 2015ap and 2016P, respectively.

Table A3. Photometry of SN 2015ap.

MJD	*U* (mag)	*B* (mag)	*V* (mag)	*R* (mag)	*I* (mag)	Telescope
57282.47	15.04 ± 0.07	15.57 ± 0.06	15.29 ± 0.09	–	–	HCT
57283.84	15.17 ± 0.06	15.63 ± 0.05	15.23 ± 0.01	15.14 ± 0.01	14.87 ± 0.01	HCT
57289.54	16.02 ± 0.08	15.94 ± 0.06	15.38 ± 0.06	–	–	ST
57290.23	–	16.43 ± 0.06	15.39 ± 0.06	15.15 ± 0.01	14.82 ± 0.01	HCT
57292.44	–	16.51 ± 0.01	15.55 ± 0.07	15.23 ± 0.01	14.85 ± 0.03	HCT
57298.92	17.84 ± 0.19	17.28 ± 0.09	16.12 ± 0.08	15.66 ± 0.01	15.24 ± 0.01	ST
57299.83	–	17.30 ± 0.17	16.18 ± 0.01	15.72 ± 0.01	15.23 ± 0.01	ST
57300.92	–	–	16.15 ± 0.01	15.92 ± 0.01	15.44 ± 0.01	ST
57302.44	18.01 ± 0.23	17.61 ± 0.11	16.33 ± 0.03	15.92 ± 0.02	15.43 ± 0.02	ST
57317.86	–	–	16.89 ± 0.02	–	16.44 ± 0.01	ST
57325.75	–	–	17.18 ± 0.36	16.82 ± 0.01	16.63 ± 0.01	ST
57330.70	–	–	–	17.12 ± 0.01	16.84 ± 0.01	ST
57331.77	–	–	17.25 ± 0.05	17.16 ± 0.01	16.84 ± 0.01	ST
57332.78	–	–	17.33 ± 0.03	17.17 ± 0.02	16.85 ± 0.02	ST
57334.72	–	–	–	17.19 ± 0.02	16.95 ± 0.01	ST
57335.86	–	–	17.39 ± 0.05	17.19 ± 0.01	16.93 ± 0.02	ST
57336.83	–	–	17.45 ± 0.04	17.19 ± 0.02	16.94 ± 0.02	ST
57341.83	–	18.26 ± 0.01	–	–	–	DFOT
57342.87	–	–	17.66 ± 0.04	–	16.96 ± 0.02	DFOT
57345.81	–	–	17.72 ± 0.02	17.28 ± 0.01	17.07 ± 0.02	ST
57353.78	–	18.29 ± 0.02	17.494 ± 0.019	–	17.24 ± 0.08	HCT
57357.83	–	18.43 ± 0.03	17.79 ± 0.02	17.53 ± 0.02	–	HCT
57361.80	–	18.54 ± 0.08	17.79 ± 0.05	–	17.29 ± 0.01	ST
57366.95	19.04 ± 0.04	18.36 ± 0.07	17.91 ± 0.06	17.82 ± 0.06	17.39 ± 0.06	Copernico
57375.35	19.42 ± 0.08	18.61 ± 0.06	17.99 ± 0.09	17.95 ± 0.09	17.39 ± 0.09	DFOT
57386.69	–	–	18.28 ± 0.03	18.19 ± 0.02	17.70 ± 0.04	ST
57387.70	–	–	18.29 ± 0.16	18.19 ± 0.02	17.72 ± 0.05	ST
57390.62	–	–	–	18.26 ± 0.03	17.78 ± 0.06	ST
57391.68	–	–	18.39 ± 0.09	–	17.79 ± 0.05	ST
57392.68	–	–	18.02 ± 0.03	18.24 ± 0.04	17.80 ± 0.05	ST
57402.68	–	18.79 ± 0.09	18.58 ± 0.13	–	17.95 ± 0.05	DFOT

Table A3 – *continued*

MJD	*U* (mag)	*B* (mag)	*V* (mag)	*R* (mag)	*I* (mag)	Telescope
57403.68	–	18.78 ± 0.06	18.59 ± 0.14	18.31 ± 0.05	18.08 ± 0.05	DFOT
57412.59	–	18.88 ± 0.02	18.69 ± 0.03	18.50 ± 0.20	18.201 ± 0.07	HCT
57415.60	–	–	–	18.48 ± 0.04	18.28 ± 0.06	ST
57417.64	–	–	18.76 ± 0.13	18.49 ± 0.05	18.30 ± 0.06	ST
57429.59	–	–	18.79 ± 0.09	18.59 ± 0.05	18.55 ± 0.01	ST
57628.04	21.93 ± 0.09	21.50 ± 0.08	21.09 ± 0.08	20.95 ± 0.08	20.86 ± 0.08	Copernico

Table A4. Photometry of SN 2016P.

MJD	*B* (mag)	*V* (mag)	*R* (mag)	*I* (mag)	Telescope
57408.00	17.71 ± 0.05	16.98 ± 0.05	16.90 ± 0.03	16.74 ± 0.02	ST
57408.98	–	–	16.69 ± 0.01	16.72 ± 0.03	ST
57409.52	17.73 ± 0.09	16.98 ± 0.08	–	16.64 ± 0.02	ST
57410.91	17.47 ± 0.06	16.90 ± 0.01	16.63 ± 0.04	16.43 ± 0.01	HCT
57419.89	18.05 ± 0.08	16.89 ± 0.09	16.41 ± 0.08	16.19 ± 0.01	HCT
57420.99	–	–	16.44 ± 0.01	16.19 ± 0.01	HCT
57422.02	–	17.02 ± 0.01	16.49 ± 0.02	16.24 ± 0.01	HCT
57424.98	–	17.21 ± 0.01	–	16.30 ± 0.01	HCT
57428.91	–	17.57 ± 0.05	16.99 ± 0.01	16.61 ± 0.03	ST
57432.00	–	17.80 ± 0.07	–	–	ST
57432.99	–	17.83 ± 0.09	17.21 ± 0.08	16.74 ± 0.06	ST
57433.89	19.02 ± 0.01	17.89 ± 0.09	17.35 ± 0.01	16.74 ± 0.01	HCT
57438.98	–	18.17 ± 0.01	17.73 ± 0.01	17.32 ± 0.03	HCT
57448.79	19.43 ± 0.01	18.31 ± 0.08	17.88 ± 0.01	17.81 ± 0.01	HCT
57451.50	19.45 ± 0.01	18.37 ± 0.07	17.99 ± 0.01	17.89 ± 0.01	HCT
57454.49	–	18.46 ± 0.09	18.05 ± 0.01	17.81 ± 0.01	DFOT
57454.74	–	18.49 ± 0.09	18.07 ± 0.01	17.86 ± 0.01	DFOT
57460.52	–	18.74 ± 0.09	18.23 ± 0.01	18.04 ± 0.02	HCT
57461.80	–	18.78 ± 0.04	18.26 ± 0.01	18.07 ± 0.01	HCT
57462.84	19.58 ± 0.02	18.81 ± 0.02	18.26 ± 0.01	18.11 ± 0.08	ST
57465.90	–	–	18.30 ± 0.01	18.23 ± 0.02	ST
57478.32	–	19.00 ± 0.01	18.50 ± 0.01	18.51 ± 0.03	HCT
57485.54	–	19.26 ± 0.01	18.67 ± 0.01	–	HCT
57486.00	–	–	–	18.90 ± 0.02	DFOT
57489.50	20.12 ± 0.07	19.31 ± 0.07	18.93 ± 0.01	18.90 ± 0.01	DFOT
57491.41	20.18 ± 0.06	19.34 ± 0.01	18.99 ± 0.01	–	HCT
57510.77	–	–	19.04 ± 0.01	19.16 ± 0.23	ST
57542.67	–	19.86 ± 0.08	19.41 ± 0.09	19.59 ± 0.01	HCT

This paper has been typeset from a TEX/LATEX file prepared by the author.